The Astrophysical Journal, 787:25 (19pp), 2014 May 20 doi:10.1088/0004-637X/787/1/25

HUBBLE SPACE TELESCOPE OBSERVATIONS AND GEOMETRIC MODELS OF COMPACT MULTIPOLAR PLANETARY NEBULAE

Chih-Hao Hsia (夏志浩), Wayne Chau (周穎鏘), Yong Zhang (張泳), and Sun Kwok (郭新)
Department of Physics, The University of Hong Kong, Pokfulam Road, Hong Kong, China; xiazh@hku.hk,
wwlljj1314@gmail.com, zhangy96@hku.hk, sunkwok@hku.hk
Received 2013 December 5; accepted 2014 March 29; published 2014 April 30

ABSTRACT

We report high angular resolution *Hubble Space Telescope* observations of 10 compact planetary nebulae (PNs). Many interesting internal structures, including multipolar lobes, arcs, two-dimensional rings, tori, and halos, are revealed for the first time. These results suggest that multipolar structures are common among PNs, and these structures develop early in their evolution. From three-dimensional geometric models, we have determined the intrinsic dimensions of the lobes. Assuming the lobes are the result of interactions between later-developed fast winds and previously ejected asymptotic giant branch winds, the geometric structures of these PNs suggest that there are multiple phases of fast winds separated by temporal variations and/or directional changes. A scenario of evolution from lobe-dominated to cavity-dominated stages is presented. The results reported here will provide serious constraints on any dynamical models of PNs.

Key words: ISM: jets and outflows – planetary nebulae: general – stars: AGB and post-AGB – stars: evolution – stars: mass-loss

Online-only material: color figures

1. INTRODUCTION

Recent high angular resolution, high dynamic range imaging of planetary nebulae (PNs), in particular those made by the *Hubble Space Telescope* (*HST*), have shown that many PNs have complicated structures. Instead of simple ellipsoidal shells or bipolar lobes, an increasing number of PNs are found to have multiple bipolar lobes, multiple shells, arcs, rings, and extended halos. Of particular interest are quadruple or multiple nebulae, which have been observed in a number of PNs including M 2-46 (Manchado et al. 1996), NGC 2440 (López et al. 1998), Hen 2-47, M 1-37 (Sahai 2000), NGC 6881 (Kwok & Su 2005), NGC 6072 (Kwok et al. 2010), NGC 6644 (Hsia et al. 2010), NGC 6058 (Gillén et al. 2013), and NGC 7026 (Clark et al. 2013). It would be interesting to observe a larger sample of objects in order to determine whether multipolar structures are isolated or part of a general phenomenon.

The existence of multipolar objects suggests that the fast outflows responsible for the shaping of PNs are not spherically symmetric, but are highly collimated. Multipolar structures have been suggested as the result of simultaneous collimated outflows in different directions, or the outflow direction has changed with time (and the term bipolar, rotating, episodic jets, BRETS, has been used to refer to these phenomenon; López et al. 1995). Precession of the mass-losing star's rotation axis and orbiting jet with time-dependent ejection velocity due to a binary or multiple sub-stellar companions has been suggested as one of the possible causes (García-Segura 1997). While it is commonly accepted that the morphological structures of PNs are shaped by wind interactions (Balick & Frank 2002), the presence of these multiple structures implies that there must be successive phases of stellar winds with temporal and directional variations. In order to determine when do these dynamical events occur, it would be useful to observe PNs that are young. In this paper, we present the observations of 10 compact (and probably young) PNs that have been found to have multipolar morphologies. The main aim is to investigate nebular intrinsic structures and their connections with other properties of PNs.

2. OBSERVATIONS AND DATA REDUCTION

Our observed sample is selected from a group of compact, low-excitation PNs with high radio surface brightness. Since the central stars of PNs evolve from low to high temperatures and the nebular density decreases as the result of expansion, these properties represent the characteristics of PNs early in their evolution (Kwok 1990).

Observations in this study are based on data obtained by the *HST* under programs 8307 (PI: S. Kwok) and 8345 (PI: R. Sahai) using the Wide Field Planetary Camera 2. Data were retrieved from the Space Telescope Science Archive. All objects were observed with the Planetary Camera, which provides a $36\farcs8 \times 36\farcs8$ field of view (FOV) at a spatial resolution of $0\farcs045$ pixel^{-1}. These objects were imaged with three narrow-band filters: F502N [O III] ($\lambda_c = 5012$ Å, $\Delta\lambda = 27$ Å), F656N Hα ($\lambda_c = 6564$ Å, $\Delta\lambda = 22$ Å), and F658N [N II] ($\lambda_c = 6591$ Å, $\Delta\lambda = 29$ Å), respectively. To allow for the imaging of both the bright central regions and the faint outer parts of the PNs, the actual observations were made with different exposure times (from 20 s to 600 s). The data were processed through the *HST* pipeline calibration. Standard flat-field correction and bias subtraction were performed. All data were taken in two-step dithered positions to enhance spatial sampling and cosmic rays removal by using the task **crrej** in the STSDAS package of IRAF. A journal of these observations is summarized in Table 1.

3. RESULTS

The processed composite-color images of our sample objects are shown in Figure 1. We find that most of the nebulae have low [O III] λ5007/Hα flux ratios, suggesting that they are low excitation objects, consistent with they being young. Central stars are detected in all nebulae except IC 5117.

From the Hα false-color and composite-color images shown in Figure 1, it is clear that these nebulae have complex structures. Most of them have multiple bipolar lobes, and some have central tori, and faint diffuse halos. Sizes of the lobes and central ionized tori are measured by fitting the ellipses to the images.

Table 1
Log of Observations

Object	Other Name	R.A. (J2000.0)	Decl. (J2000.0)	Filter	Exposures (s)	Observation Date	Program ID
H 1-54	PNG 002.1-04.2	18:07:07.24	−29:13:06.4	F656N	140 × 2, 460 × 2	1999 Aug 21	8345
Hen 2-86	PNG 300.7-02.0	12:30:30.48	−64:52:05.7	F656N	20, 300 × 2	1999 Sep 24	8345
				F658N	20, 230 × 2	1999 Sep 24	8345
Hen 2-320	PNG 352.9-07.5	18:00:11.82	−38:49:52.7	F656N	20, 230 × 2	1999 Aug 23	8345
				F658N	20, 300 × 2	1999 Aug 23	8345
Hen 2-447	PNG 057.9-01.5	19:45:22.16	+21:20:03.9	F502N	600 × 3	1999 Nov 09	8307
				F656N	260 × 2	1999 Nov 09	8307
				F658N	500 × 2	1999 Nov 09	8307
IC 5117	PNG 089.8-05.1	21:32:30.97	+44:35:47.5	F502N	160 × 2	1999 Nov 02	8307
				F656N	120 × 2	1999 Nov 02	8307
				F658N	300 × 2	1999 Nov 02	8307
M 1-30	PNG 355.9-04.2	17:52:58.95	−34:38:23.0	F656N	20, 300 × 2	2000 Feb 23	8345
				F658N	20, 230 × 2	2000 Feb 23	8345
M 1-59	PNG 023.9-02.3	18:43:20.20	−09:04:49.1	F656N	20, 300 × 2	1999 Sep 24	8345
				F658N	20, 230 × 2	1999 Sep 24	8345
M 1-61	PNG 019.4-05.3	18:45:55.12	−14:27:37.9	F502N	160 × 2	1999 Nov 08	8307
				F656N	120 × 2	1999 Nov 08	8307
				F658N	260 × 2	1999 Nov 08	8307
M 3-35	PNG 071.6-02.3	20:21:03.77	+32:29:24.0	F502N	520 × 2	1999 Nov 04	8307
				F656N	260 × 2	1999 Nov 04	8307
				F658N	600 × 3	1999 Nov 04	8307
NGC 6790	PNG 037.8-06.3	19:22:56.97	+01:30:46.5	F502N	160 × 2	1999 Oct 31	8307
				F656N	80 × 2	1999 Oct 31	8307
				F658N	350 × 2	1999 Oct 31	8307

The measured parameters of these features including their sizes, position angles (P.A.s) of major axes, and derived inclination angles (i) are listed in Table 2.

3.1. Individual Objects

Generally, these PNs show two to four pairs of lobes and a spherical faint halo although their appearances are diverse. The detailed descriptions of individual PNs are given as follows.

H 1-54 (PNG 002.1-04.2). Although H 1-54 seems to have an ordinary, unspectacular structure in low-resolution images, our *HST* image of this object has revealed very interesting internal structures (Figure 1). There is a bright core, four pairs of bipolar lobes, an outer halo, and a circular outer arc. The largest measured dimension of the object is about 3″ measured from our *HST* Hα image. Four pairs of bipolar lobes oriented at different directions can clearly be seen. These lobes seem to originate from a common origin within the bright central core and extend out to the limit of the outer halo. At the outer northern edge of the nebula is a faint arc-like filament with a radius of about 1.″93. This arc traces out a well-defined boundary from N to NW, suggesting that it may be a bow-shocked structure. The possibility of this arc being the result of interaction with the interstellar medium is supported by the direction of proper motion of H 1-54 (P.A. = 1°; Roeser et al. 2010).

Hen 2-86 (PNG 300.7-02.0). Previous optical spectroscopy has classified Hen 2-86 as a type I PN (de Freitas Pacheco et al. 1992). The central star of Hen 2-86 is classified as type WC4 (Girard et al. 2007), with a Zanstra temperature of 67,000–88,000 K (Gleizes et al. 1989). Górny et al. (1999) found that nebula to have a size of 12″ × 8″ with strong Hα emission. From our high-resolution *HST* image reveals two pairs of bipolar lobes aligned roughly along the northeast (NE) to southwest (SW) direction. The inner pair of lobes has a size of 3.″25 × 1.″13 (lobe $a - a'$) and an outer pair has a size 10.″45 × 1.″28 (lobe $b - b'$). This structure is similar to that of Hen 2-320 (Figure 1) and could be related to the class of quadrupolar PNs such as M 2-46 (Manchado et al. 1996) and IPHASX J012507.9+635652 (Mampaso et al. 2006). Around the waist of the bipolar lobes is an ionized torus of well-defined shape. A faint halo can also be seen.

Hen 2-320 (PNG 352.9-07.5). At first glance, Hen 2-320 seems to be a typical bipolar nebula with a size of ∼10″. However, closer examination of our *HST* image suggests the presence of up to four pairs of bipolar lobes aligned approximately along the same bipolar axis (Figure 1). The origin of these multi-layer bipolar lobes is unclear. One possibility is that they represent episodic ionization fronts with time variation as the result of multiple interactions by successive stellar winds with a homogeneous quiescent circumstellar envelope.

In the [N II] image shown in the insert, we can see a number of co-axial rings, two in the eastern lobe and two in the western lobes. These four rings have been fitted by eye and are marked as e, f, g, h in the insert gray scale panels. The sizes of the two-dimensional (2D) rings and the P.A.s of the major axes of these rings have also presented in Table 2. Three inner rings (e, f, g) are close to the central part of this object, whereas the outer ring (h) is far to the central region. Based on the measurements and visual inspection, we can consider the ring f to be the counterpart of g. Assuming that these rings are the parts of tilted circles, the inclination angles (i) of the three inner rings (e, f, g) are approximately 11° (0° being edge-on). The measured separation between ring e and f is 0.″18. Similar structures (bipolar lobes with multiple rings) can also be found in the PN M 2-9, Hb 12 (Kwok & Hsia 2007) and Hen 2-104 (Corradi et al. 2001). These rings had been suggested to be the manifestation of a time-variable, collimated fast wind along the polar directions of bipolar lobes interact with surrounding asymptotic giant branch (AGB) circumstellar medium.

Hen 2-447 (PNG 057.9-01.5). This object shows a bright compact core (0.″84 × 0.″96) elongated at P.A. ∼ 146°. Easily discernible are two bright, extended pairs of lobes (labeled as

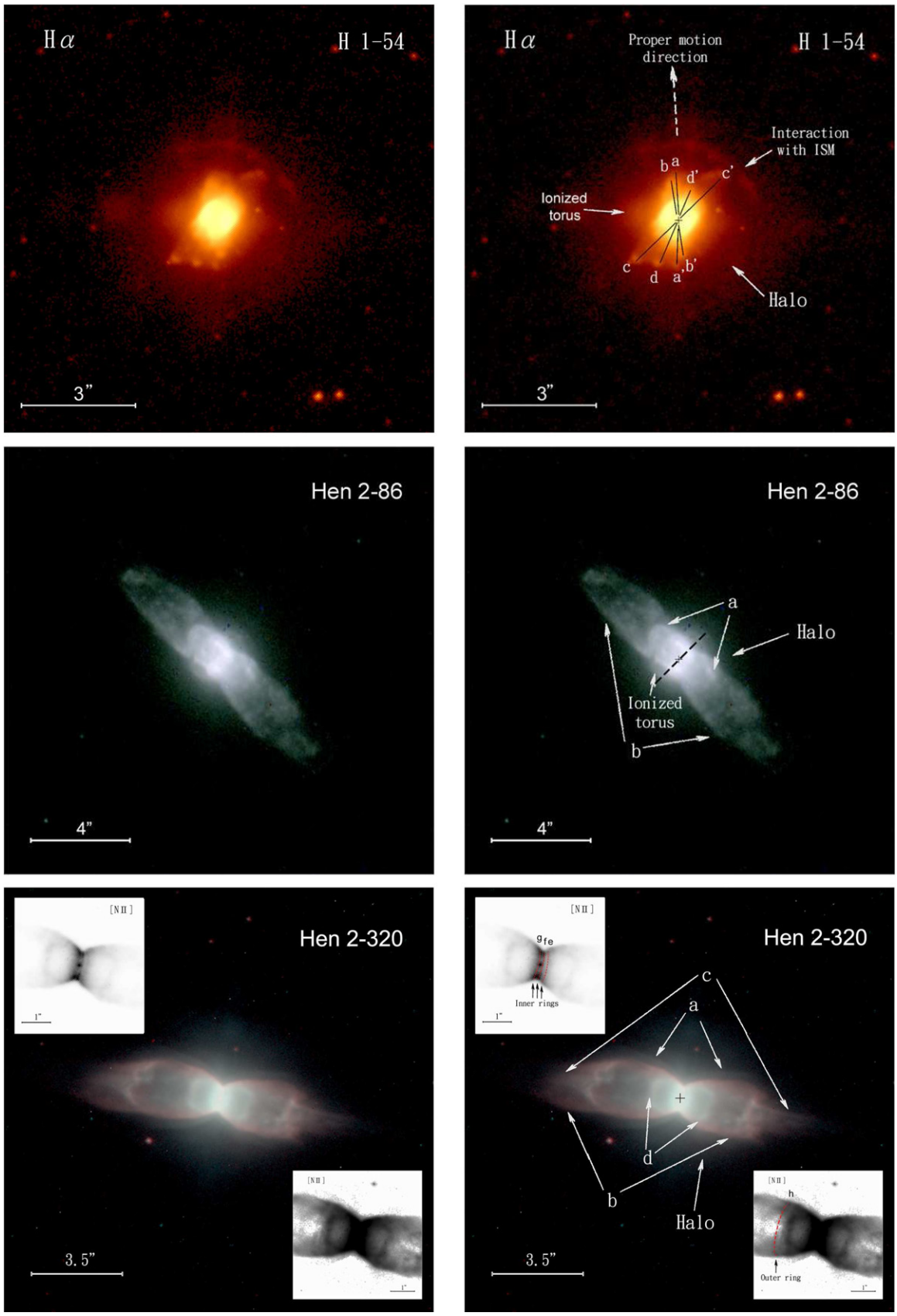

Figure 1. *HST* Hα false-color and composite-color images of 10 compact, multipolar PNs. The composite images were mainly made from three bands: [O III] (shown as blue), Hα (green), and [N II] (red), except Hen 2-86, Hen 2-320, and M 1-30 in which blue is Hα, green is Hα+[N II], and red is [N II]. The right panels are the same with the left panels but with the morphological features labeled. The positions of the central star are marked with crosses. The black dotted lines denote the position angles of the minor axes of the bipolar structures. The locations of the 2D rings are marked with red dotted lines. All images are displayed in logarithmic scales. North is up and east is to the left.

(A color version of this figure is available in the online journal.)

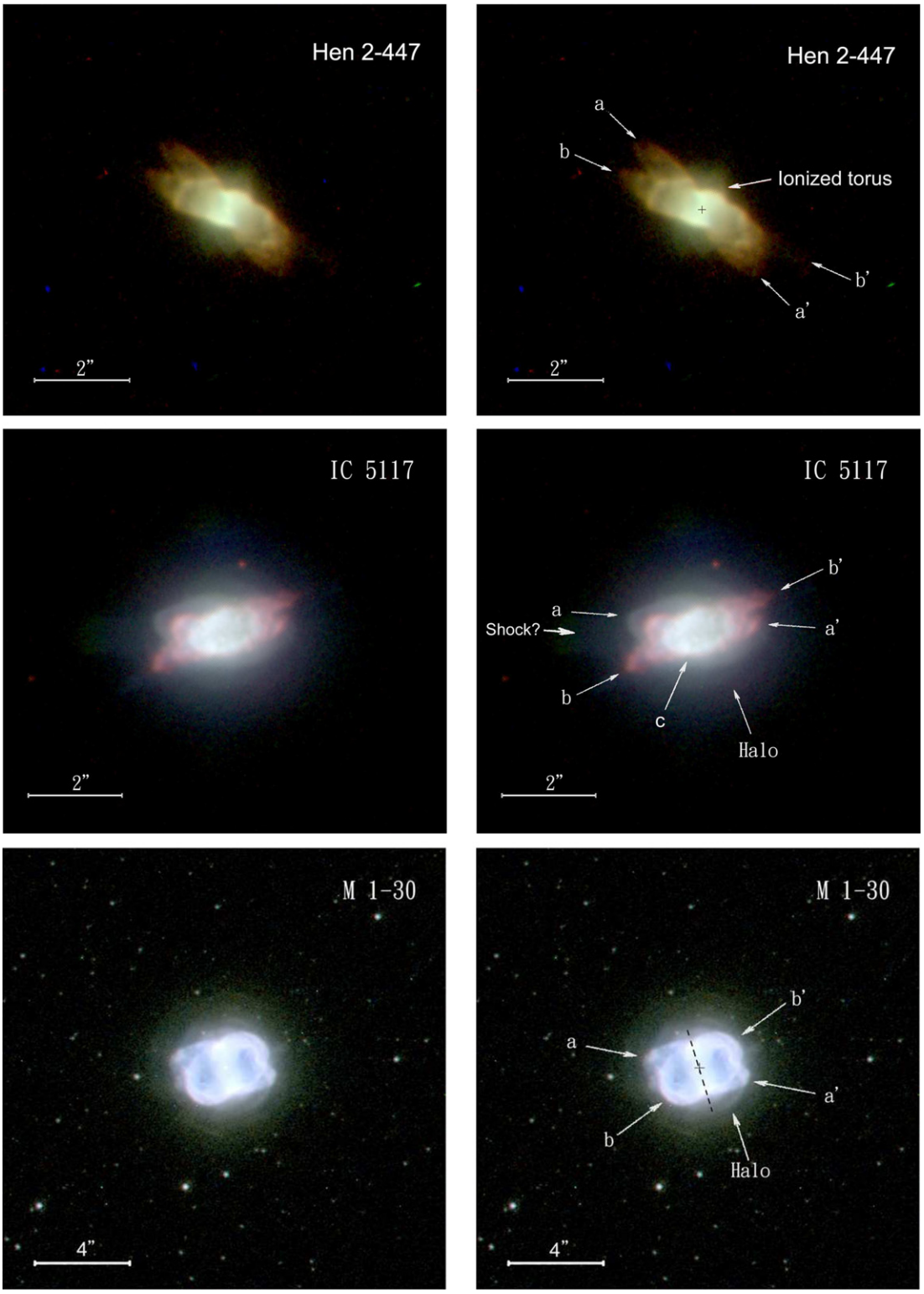

Figure 1. (Continued)

$a - a'$ and $b - b'$) with angular sizes of 4.″28 × 0.″71 and 4.″80 × 0.″85 along the approximately northeast (NE) to southwest (SW) direction. The waist of this nebula is surrounded by an extensive ionized torus with strong Hα emission. We note that the major axis and minor axis are not perpendicular for this nebula. Similar structures can also be seen in the young PN NGC 6881 and in some quadrupolar PNs such as M 2-46, K 3-24, and M 1-75 (Manchado et al. 1996). The origin of such asymmetries is still a mystery, although precession of the central source has been suggested as the cause (Guerrero & Manchado 1998; Kwok & Su 2005).

The 5 GHz and 8.4 GHz radio images of this object both show a bipolar morphology with a bright central torus (Aaquist & Kwok 1990; Kwok & Aaquist 1993). A slight *S*-shaped structure, with the eastern extension curving toward the north and the western extension curving to the south, can be seen. This is probably the result of two pairs of bipolar lobes, as can be seen clearly in the *HST* image.

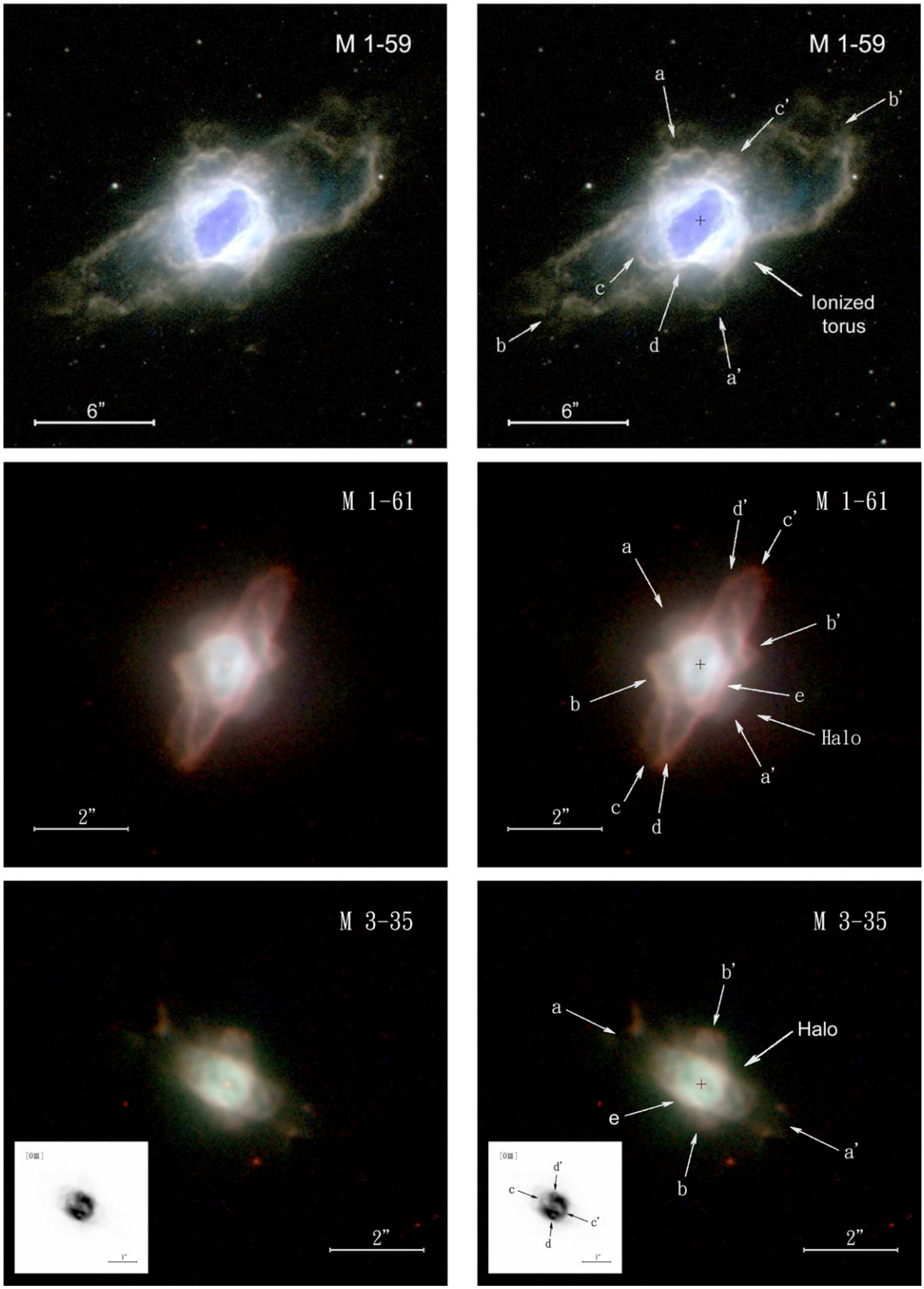

Figure 1. (Continued)

IC 5117 (PNG 023.9-02.3). This object appears to be a very dense nebula with higher excitation (Aller & Czyzak 1983). The nebula consists of a bright inner shell (labeled as *c*) with a size of 1.″68 × 1.″16 and two pairs of bipolar lobes (marked as $a - a'$ and $b - b'$) (Figure 1). An extended spherical diffuse halo can be seen in the Hα and [N II] images. We note that a faint, extended structure with a shocked-like boundary is aligned along the direction of lobe $a - a'$.

The 15 GHz radio image of IC 5117 shows a deep central emission minimum and two bright peaks along the north and

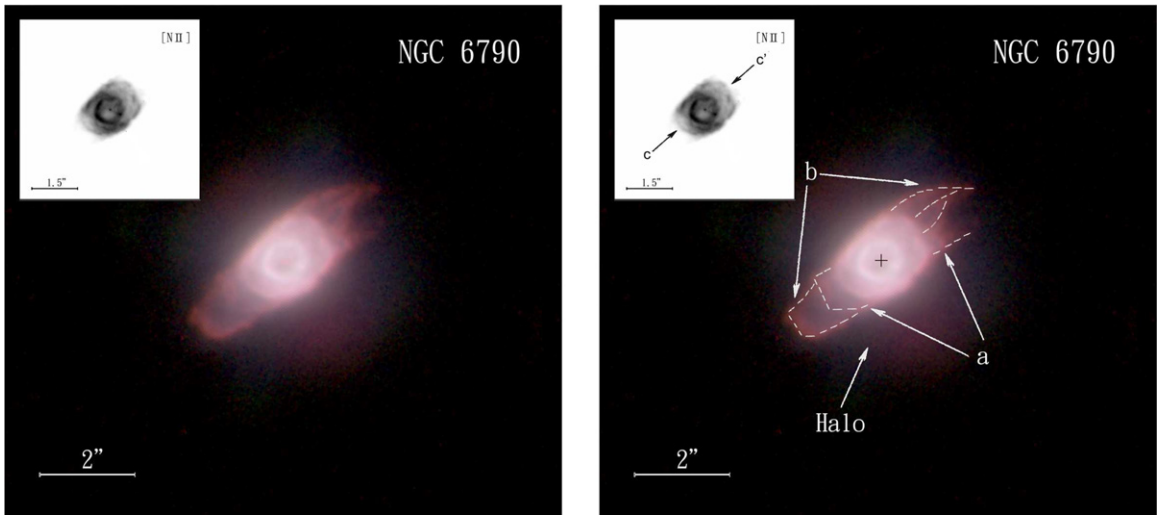

Figure 1. (Continued)

Table 2
Measured Parameters of Observed Features

Feature	H 1-54			Hen 2-86			Hen 2-320			Hen 2-447	
	Size (″)	P.A. (°)	i (°)	Size (″)	P.A. (°)	i (°)	Size (″)	P.A. (°)	i (°)	Size (″)	P.A. (°)
$a-a'$	2.61 × 0.53	2 ± 2	···	3.25 × 1.13	49 ± 3	···	5.97 × 2.02	79 ± 4	···	4.28 × 0.71	44 ± 2
$b-b'$	2.06 × 0.37	8 ± 3	···	10.45 × 1.28	46 ± 3	···	9.90 × 1.39	81 ± 3	···	4.80 × 0.85	65 ± 3
$c-c'$	3.15 × 0.49	134 ± 2	···	···	···	···	8.47 × 1.39	80 ± 3	···	···	···
$d-d'$	2.39 × 0.28	154 ± 3	···	···	···	···	2.52 × 1.39	75 ± 3	···	···	···
e	···	···	···	···	···	···	1.08 × 0.22	168 ± 2	12 ± 3[a]	···	···
f	···	···	···	···	···	···	0.91 × 0.19	168 ± 2	12 ± 3[a]	···	···
g	···	···	···	···	···	···	0.95 × 0.16	168 ± 2	10 ± 3[a]	···	···
h	···	···	···	···	···	···	2.08 × 0.98	164 ± 3	28 ± 3[a]	···	···
Ionized torus	2.91 × 1.58	88 ± 3	33 ± 3[a]	2.66 × 1.44	137 ± 3	···	···	···	···	···	···

Feature	IC 5117			M 1-30			M 1-59			M 1-61	
	Size (″)	P.A. (°)	i (°)	Size (″)	P.A. (°)	i (°)	Size (″)	P.A. (°)	i (°)	Size (″)	P.A. (°)
$a-a'$	3.03 × 0.68	88 ± 2	···	4.58 × 1.40	78 ± 2	···	7.75 × 3.55	15 ± 3	···	2.89 × 1.13	34 ± 3
$b-b'$	3.55 × 0.46	115 ± 3	···	4.06 × 1.94	129 ± 4	···	18.04 × 3.74	120 ± 4	···	2.22 × 1.04	112 ± 4
$c-c'$	···	···	···	···	···	···	6.78 × 2.54	130 ± 3	···	5.04 × 0.98	149 ± 3
$d-d'$	···	···	···	···	···	···	···	···	···	4.80 × 0.74	162 ± 3
Minor axis	···	···	···	···	17 ± 3	···	···	···	···	···	···
Inner ring	···	···	···	3.48	···	···	···	···	···	···	···
Outer ring	···	···	···	4.22	···	···	···	···	···	···	···
Jet	···	···	···	4.52	109 ± 3	···	···	···	···	···	···

Feature	M 3-35			NGC 6790		
	Size (″)	P.A. (°)	i (°)	Size (″)	P.A. (°)	i (°)
$a-a'$	2.86 × 1.24	58 ± 3	···	4.15 × 0.98	118 ± 3	···
$b-b'$	2.30 × 0.78	170 ± 4	···	4.68 × 1.06	133 ± 4	···
$c-c'$	0.8	60 ± 3	···	1.16 × 0.89	119 ± 2	50 ± 3[a]
$d-d'$	0.69	172 ± 3	···	···	···	···

Note. [a] Derived from the major–minor axis ratio assuming the orientation angle of sky plane is 90°.

south sides of this object (Aaquist & Kwok 1991; Lee & Kwok 2005). The radio image corresponds to the central shell in the *HST* image, but the two pairs of bipolar lobes and the halo are not detected in the radio image, probably due to the low dynamic range of the radio observations. The radio structure has been ascribed to a prolate ellipsoidal shell projected onto the plane of the sky (Aaquist & Kwok 1991). The extinction map of this nebula shows a similar distribution to that of the radio map, with two extinction peaks fall slightly outside the radio peaks, which indicates that the major axis of the object is rotated toward us by ∼40° (Lee & Kwok 2005).

M 1-30 (PNG 355.9-04.2). The main structure of M 1-30 consists a double bright shells which can be interpreted as a pair of bipolar lobes ($b-b'$) inclined w.r.t. the plane of the sky.

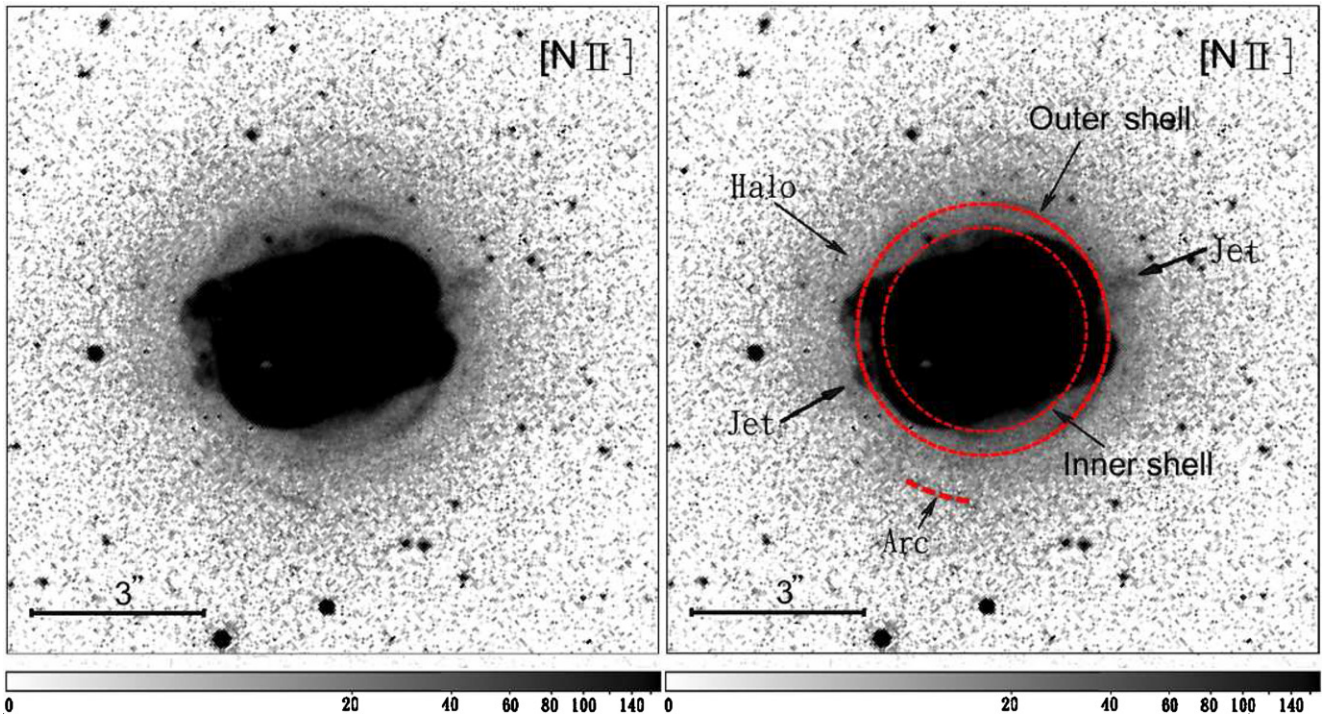

Figure 2. *HST* [N II] images of M 1-30 after the application of an unsharp mask in order to better show the faint outer structures. The right panel has the same FOVs as the left panel, but with morphological features are marked. The inner and outer shells are marked with red dotted and solid lines, respectively. North is up and east is to the left. The intensity display is on a logarithmic scale and the gray scale bar is given at the bottom in units of counts per pixel.

(A color version of this figure is available in the online journal.)

The measured angular size of this pair of lobes is $4\farcs06 \times 1\farcs94$ oriented at P.A. $= 129°$. Another pair of bipolar lobes ($a - a'$) can be seen at P.A. $= 78°$ with an angular size of $4\farcs58 \times 1\farcs40$. Outside of the main nebula is a faint, extended halo with a size of $\sim 7''$, which shows strong Hα emission.

After the application of an unsharp mask to the [N II] image, additional outer structure can be seen (Figure 2). These include two concentric shells, an arc, and one pair of collimated jets. Two concentric rings (hereafter called the inner shell and outer shell) and the arc both show the apparent ridges at their edges in the Hα and [N II] images. The measured angular radii of inner shell, outer shell, and the arc are $1\farcs74$, $2\farcs11$, and $2\farcs87$, respectively. Similar multiple shell structures have been seen in other PNs such as NGC 6543, NGC 7027 (Terzian & Hajian 2000), NGC 40, NGC 1535, and NGC 3918 (Corradi et al. 2004). These multiple shells of enhanced brightness represent results of higher density and are probably manifestations of periodic mass loss during the AGB. These are different from the 2D rings observed in Hen 2-320, which are caused by time-variable fast winds.

A pair of collimated jets with a size of $4\farcs52$ can also be seen in Figure 2. The orientation of this structure is at P.A. $= 109°$, which is located between the two prominent lobes discussed earlier. We also note that the major axis of the jets and the minor axis of this nebula seem to be perpendicular. It is possible that the pair of jets could be a third pair of lobes which are aligned nearly along the plane of the sky.

M 1-59 (PNG 023.9-02.3). M 1-59 is usually classified as a bipolar nebula but examination of our *HST* image of this object shows a much more complex structure. There are at least three pairs of closed-end bipolar lobes (labeled as $a - a'$, $b - b'$, and $c - c'$ in Figure 1), the largest of which ($b - b'$) has an angular extent of $\sim 18''$. In the center of the nebula is a hollow shell (or cavity, marked as d) with a size of $5\farcs42 \times 4\farcs64$. As in the case of IC 5117, this central hollow shell could be a result of the projection of the fourth pair of lobes which are aligned nearly along the line of sight, or a bubble created by the shocked fast wind from the central star.

A H_2 2.12 μm image of M 1-59 shows a bright central region with emission in the lobes (Guerrero et al. 2000). The 5 GHz radio image of the object (Aaquist & Kwok 1990) shows a distinctly bilobate appearance with a central emission minimum and two bright radio peaks, which indicates an elongation toward the NW–SE direction along the major axis.

M 1-61 (PNG 019.4-05.3). M 1-61 is a clear multipolar nebula with at least four pairs of bipolar lobes (Figure 1). Two pairs of lobes ($c - c'$, and $d - d'$) are nearly aligned with each other but the other pair ($a - a'$, and $b - b'$) probably represents lobes with axes highly inclined w.r.t. the plane of the sky. A ellipsoidal central shell (marked as e) can also be seen.

The 15 GHz radio images show a shell-like structure with two prominent peaks with roughly the same brightness aligned along the E–W direction (Aaquist & Kwok 1991; Lee & Kwok 2005). These two bright peaks are also apparent in the 5 GHz map (Aaquist & Kwok 1990).

M 3-35 (PNG 071.6-02.3). M 3-35 is a medium excitation PN with a central star temperature of ~60,000 K (Kaler 1986). Our *HST* image shows two pairs of bipolar lobes (marked as $a - a'$ and $b - b'$ in Figure 1) with different orientations and a bright central shell (labeled as e) of size of $0\farcs55 \times 0\farcs64$. The orientation angles of the two bipolar lobes are measured to be P.A. $= 58° \pm 3°$ and $170° \pm 4°$ for lobes $a - a'$ and $b - b'$, respectively. The two bipolar lobes have similar projected sizes on the sky, with $a - a'$ having a size of $\sim 2\farcs86$ and $b - b'$ a size of $\sim 2\farcs30$.

In the [O III] image (shown in the insert), two pairs of cavities ($c - c'$ and $d - d'$) associated with the bipolar lobes $a - a'$ and $b - b'$ are also found in the central region. These two pairs of

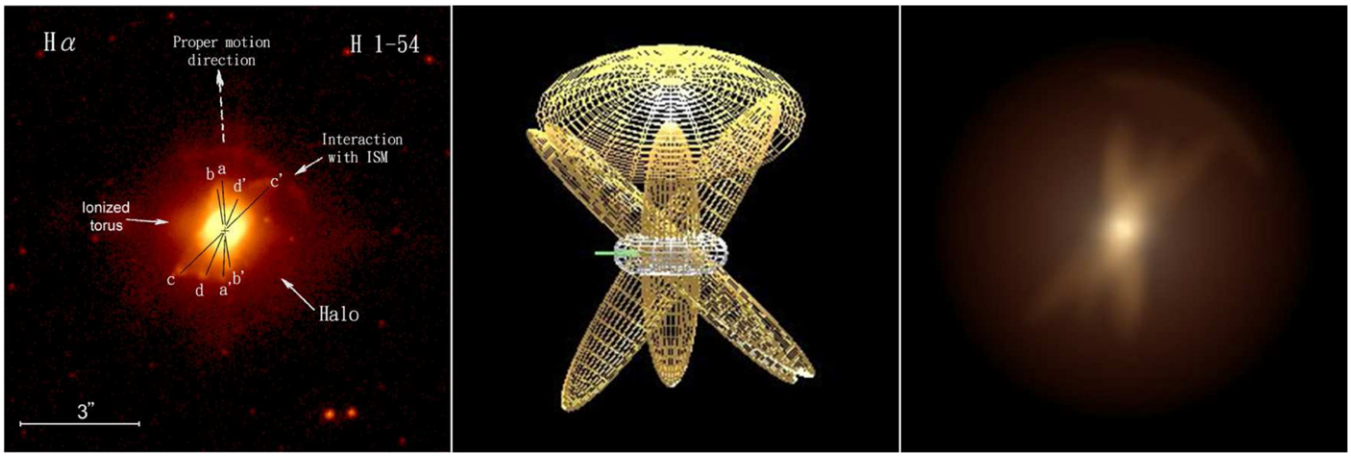

Figure 3. *HST* image (left), three-dimensional mesh (center), and rendered image (right) of H 1-54. The mesh of the model is oriented to best display the three-dimensional morphology and is not related to the actual orientation of the PN with respect to the plane of the sky. The scattering halo is not shown in the mesh. A Gaussian blur has been applied to the rendering.

(A color version of this figure is available in the online journal.)

cavities have symmetry axes that lie at the P.A.s of $60^\circ \pm 3^\circ$ and $172^\circ \pm 3^\circ$, which are closely aligned with the orientations of the two pairs of bipolar lobes.

The 15 GHz radio continuum images clearly resolve the central region of this nebula (Aaquist & Kwok 1991; Lee & Kwok 2005). A deep central emission minimum and a double-peaked structure with roughly the same brightness are aligned along the minor axis of the $a - a'$ bipolar lobes in the optical image. The radio structure can be modeled by a prolate ellipsoidal shell with the major axis rotated toward us by $\sim 60^\circ$ (Aaquist & Kwok 1991). Lee & Kwok (2005) also found that the extinction map of this object has similar distribution to that of the radio map, which shows the locations of high extinction regions coinciding with the double-peaked structure. A comparison of the optical [O III] enlarged image and dust extinction map (Lee & Kwok 2005) of this nebula, we can see that the cavity $d - d'$ and two high-extinction regions have approximately the same locations. It is possible that the presence of lobe $b - b'$ could be the result of illumination through the cavity $d - d'$ in the equatorial torus.

NGC 6790 (PNG 037.8-06.3). NGC 6790 is another nebula seen with multi-layer shells. There are two outer bipolar lobes (labeled as $a - a'$ and $b - b'$) with axes along the NW–SE direction. The two inner shells (marked as c and c') are shown in more detail in the insert [N II] image. The symmetry axes of lobes $a - a'$ and $b - b'$ have P.A.s of $118^\circ \pm 3^\circ$ and $133^\circ \pm 4^\circ$, respectively. The major axes of the two inner shells are similar, both oriented at P.A. $= 119^\circ \pm 2^\circ$. Similar structures can be seen in other multipolar PN such as NGC 6644 (Hsia et al. 2010) and He 2-47 (Sahai 2000). These structures probably represent the presence of another pair of lobes aligned nearly along the line of sight. If the projection of the third pair of lobes (referred to as lobe $c - c'$) is indeed composed of these two inner shells, then we can derive an inclination angle of about 50° for the lobe $c - c'$ (assuming the orientation of sky plane is 90°).

While the *HST* image shows an elongated structure with a major axis dimension of $\sim 5''$, the 5 GHz and 15 GHz ratio images are roughly circular with a diameter of $\sim 2''$. The slight elongation along the NW–SW direction has been suggested to be the result of the nebula being density bounded along this direction (Aaquist & Kwok 1990, 1991). This is consistent with the present *HST* observations, where the nebula is seen to be density bounded along the bipolar axis but ionization bounded elsewhere. A faint, extended halo with a well-defined spherical shape (with a size of $\sim 6\farcs54$) can also be seen, which are consistent with the size measured by Hua et al. (1993).

4. THE MODELS

It is clear from Section 3 that the structures of these PNs are complex. Because of the presence of emission lines, young PNs are much brighter optically than proto-PNs, which shines by dust-scattered starlight. It is therefore much easier to see the fainter structures in young PNs than proto-PNs. We would like to take advantage of the excellent quality of these *HST* images to discern the intrinsic structures of the nebulae. In order to achieve this goal, we have performed three-dimensional (3D) modeling using the software package *Shape* (Steffen et al. 2011) and compare the rendered model images with observed images. Using the observed images as a guide, we have created models of multiple bipolar lobes as a starting point. The sizes and orientations of the lobes are given in Table 3. The surface brightness of the simulated images represented integrated emission measures ($\int n_e^2 d\ell$) along the line of sight.

H 1-54. As discussed in Section 3, the *HST* image of H 1-54 (shown in the left panel of Figure 3), shows four pairs of bipolar lobes, an ionized torus in the central region, a halo component, and an arch-shaped feature. To model this PN, it has been assumed that all the bipolar elements in the PN are identical and the differences in their apparent lengths are entirely attributed to the projection effect. Since no shell-like structure is seen in the observed image, the elements in the model are given a uniform density distribution. The arc feature is emulated using a thin, incomplete spherical shell that spans 80°. A 3D mesh is also provided in the center panel of Figure 3 to aid visualization of the morphology. As seen from the rendered image in the right panel of Figure 3, in which a Gaussian blur has been applied to account for the telescope beam, the model is able to generate images that closely resemble the observed image.

Hen 2-86. From the *HST* image displayed in the left panel of Figure 4, three elements can be identified in the PN: an outer pair of bipolar lobes, an inner pair of bipolar lobes and an ionized torus. Under the assumption that both the outer and inner bipolar elements lie more or less in the plane of the sky, the elements are created according to measurements listed in

Table 3
Parameters of *Shape* Models[a,b]

Object Name	Component	Component Morphology	Absolute Dimensions ($l'' \times w''/r_e, r_i$)	Density Distribution	P.A. (°)	Inc. (°)
H 1-54	$a-a'$	Bipolar	3.20 × 0.50	Uniform	2	34
	$b-b'$	Bipolar	3.20 × 0.50	Uniform	8	−49
	$c-c'$	Bipolar	3.20 × 0.50	Uniform	−44	0
	$d-d'$	Bipolar	3.20 × 0.50	Uniform	−26	−41
	ISM Interaction	Incomplete shell	3.52, 3.36	Uniform	−30	0
	Ionized Region	Toroidal[c]	0.96, 0.32	Uniform	−5	0
Hen 2-86	a	Bipolar (55% squeeze)	3.22 × 1.12	Uniform	46	0
	b	Bipolar (50% squeeze)	10.4 × 1.25	Uniform	49	0
	Ionized Region	Toroidal[c]	1.56, 0.52	Uniform	47	0
Hen 2-320	a	Bipolar (50% squeeze)	5.94 × 2.08	Shell	79	0
	b	Bipolar (50% squeeze)	8.47 × 1.39	Shell	80	0
	c	Bipolar (50% squeeze)	9.90 × 1.39	Shell	81	0
	d	Bipolar (75% squeeze)	1.58 × 0.99	Shell	90	0
Hen 2-447	$a-a'$	Bipolar (20% squeeze)	4.80 × 0.85	Shell	44	−63
	$b-b'$	Bipolar (20% squeeze)	4.80 × 0.85	Shell	80	0
IC 5117	$a-a'$	Bipolar (20% squeeze)	3.60 × 0.72	Shell	88	0
	$b-b'$	Bipolar (20% squeeze)	3.60 × 0.72	Shell	115	31
	c	Bipolar	1.80 × 0.95	Uniform	−75	30
M 1-30	$a-a'$	Bipolar (50% squeeze)	4.60 × 1.41	Shell	78	0
	$b-b'$	Bipolar (20% squeeze)	4.09 × 1.95	Shell	−51	0
M 1-59	$a-a'$	Bipolar	18.0 × 3.53	Shell	15	65
	$b-b'$	Bipolar	18.0 × 3.73	Shell	−60	0
	$c-c'$	Bipolar	18.0 × 2.51	Shell	−50	68
	$d-d'$	Bipolar	18.0 × 3.73	Shell	−50	80
	Ionized region	Toroidal[c]	4.50, 1.80	Uniform	−10	−70
M 1-61	$a-a'$	Bipolar	5.00 × 0.73	Shell	34	70
	$b-b'$	Bipolar	5.00 × 1.03	Shell	−68	64
	$c-c'$	Bipolar	5.00 × 0.97	Shell	−31	0
	$d-d'$	Bipolar	5.00 × 1.12	Shell	−18	−18
	e	Bipolar (pole-on)	5.00 × 0.73	Shell	−2	−82
M 3-35	$a-a'$	Bipolar	2.70 × 1.17	Shell	59	0
	$b-b'$	Bipolar	2.70 × 1.17	Shell	−10	36
	e	Bipolar	2.70 × 1.17	Shell	60	74
NGC 6790	$a-a'$	Bipolar	4.70 × 0.98	Shell	−62	−27
	$b-b'$	Bipolar	4.70 × 1.07	Shell	−47	0
	$c-c'$	Bipolar	1.81 × 0.89	Shell	−61	50

Notes.
[a] Emission intensity of the *Shape* models are proportional to n^2, where n is the number density of emitters. Unless otherwise specified, emitters are distributed on the surface of the listed components in a shell of finite thickness. For certain objects, the distribution of emitter may also follow an angular dependency as specified in the text.
[b] P.A. is defined from the north rotating eastward and Inc. referenced to the plane of the sky.
[c] P.A. and Inc. of toroidal components referenced to the axis of rotational symmetry. Absolute dimensions of toroidal components are specified by r_e and r_i, which are respectively the internal and external radius.

Table 2. Also added to the bipolar lobes is a slight tightening at their waists—a property that is evident in the *HST* image. Like H 1-54, no shell structure is apparent; hence, the elements in the model are given a uniform density distribution. A 3D mesh of the model is presented in the center panel of Figure 4 with the numerical details of the model provided in Table 3. We can see that the *Shape* rendered image in the right panel of Figure 4 shows a good resemblance to the observed image.

Hen 2-320. The lobes of this nebula show shell-like structures and we assume a thin (0.″1) shell geometry for all the four bipolar lobes identified in the left panel of Figure 5. All four pairs of lobes are assumed to all reside on the plane of the sky, and a waist tightening has been applied to the model. Parameters of the model are derived from the measurements in Table 2 are listed in Table 3.

Hen 2-447. Like Hen 2-320, the bipolar lobes of Hen 2-447 appear to have a shell-like structure as seen in the *HST* image displayed in the left panel of Figure 6. Initial inspection of the observed image suggests three bipolar elements, which can easily be mimicked using three pairs of identical bipolar lobes oriented at different P.A.s and inclinations. Interestingly, further investigation reveals that two bipolar components are already sufficient to produce a rendering (right panel of Figure 6) that is consistent with observations. The bright region in between the two lobes $a-a'$ and $b-b'$ can be accounted for by the intersecting regions of the two bipolar lobes. This model is

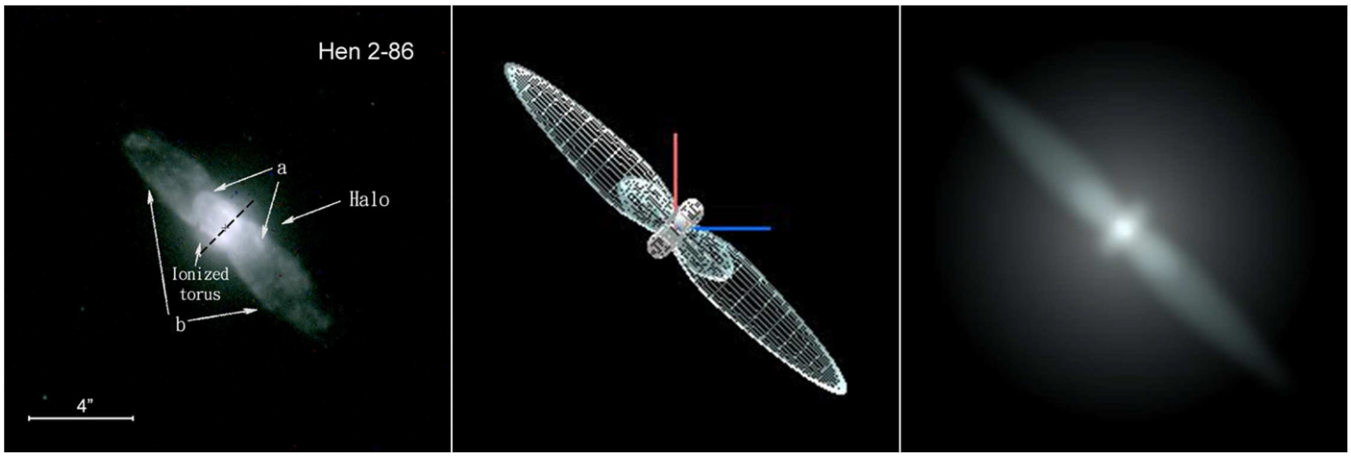

Figure 4. *HST* image (left), three-dimensional mesh (center), and rendered image (right) of He 2-86. The scattering halo is not shown in the mesh. A Gaussian blur has been applied to the rendering.

(A color version of this figure is available in the online journal.)

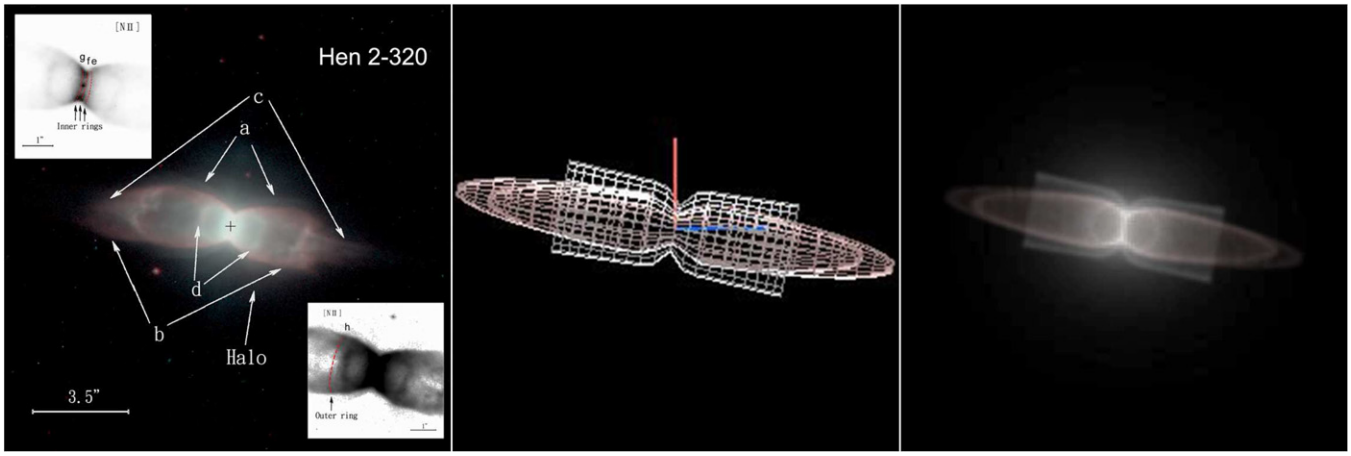

Figure 5. *HST* image (left), three-dimensional mesh (center), and rendered image (right) of He 2-320. The scattering halo and the innermost bipolar element are not shown in the mesh. A Gaussian blur has been applied to the rendering.

(A color version of this figure is available in the online journal.)

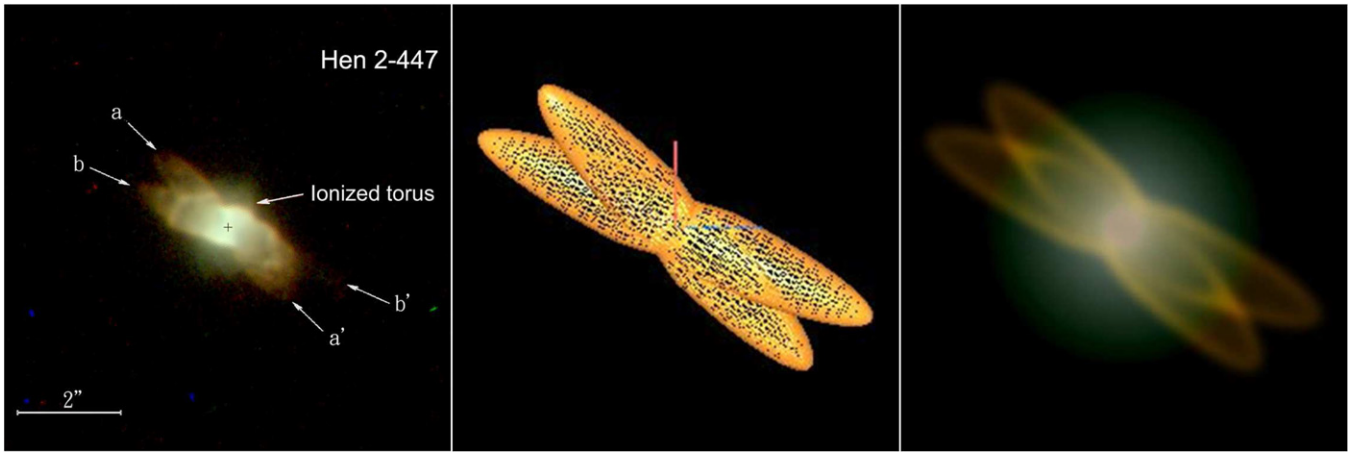

Figure 6. *HST* image (left), three-dimensional mesh (center), and rendered image (right) of He 2-447. The scattering halo is not shown in the mesh. A Gaussian blur has been applied to the rendering.

(A color version of this figure is available in the online journal.)

particularly enlightening as it demonstrated that features interpreted as a separate component can easily arise from the overlap of other components. Signification simplification in PN models can result from similar interpretation of observed feature.

IC 5117. Clearly identifiable from the *HST* image of IC 5117 in the left panel of Figure 7 are two pairs of bipolar lobes. As they display a shell-like appearance, these bipolar features are likely to be cavities. In the model, these cavities are assumed

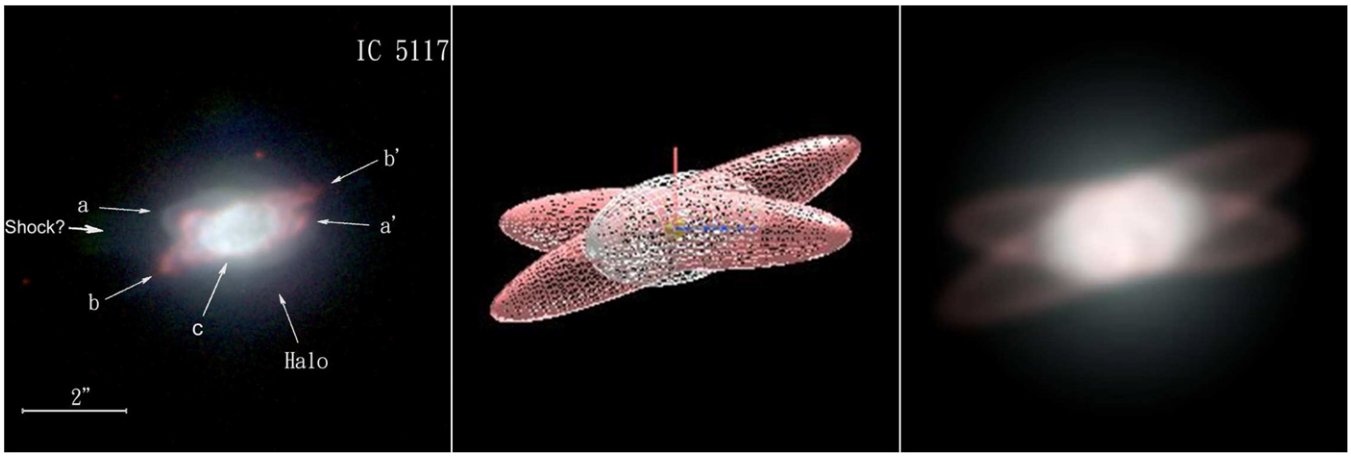

Figure 7. *HST* image (left), three-dimensional mesh (center), and rendered image (right) of IC 5117. The scattering halo is not shown in the mesh. A Gaussian blur has been applied to the rendering.

(A color version of this figure is available in the online journal.)

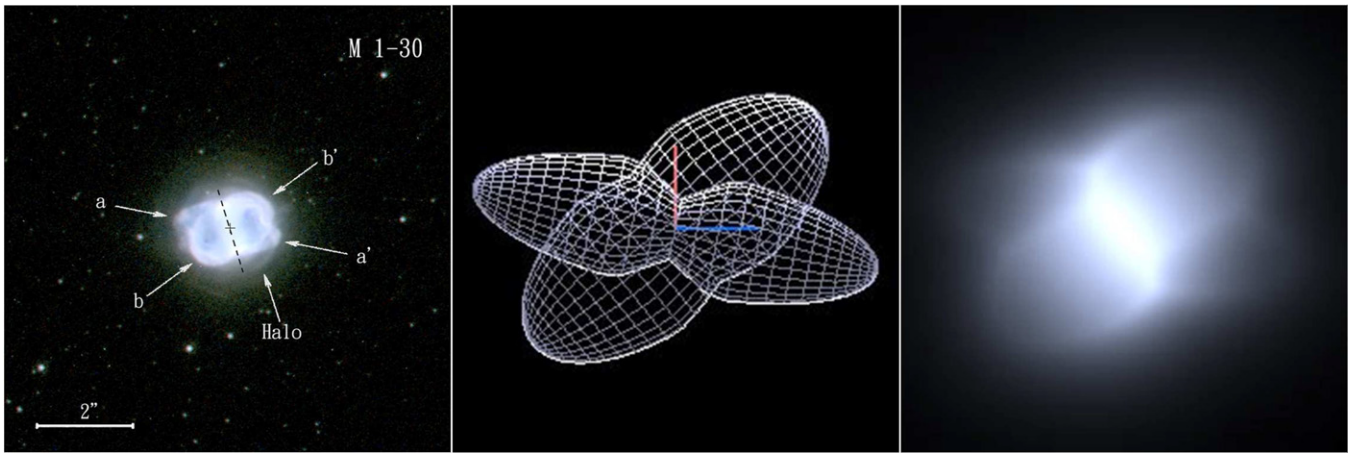

Figure 8. *HST* image (left), three-dimensional mesh (center), and rendered image (right) of M 1-30. The scattering halo is not shown in the mesh. A Gaussian blur has been applied to the rendering.

(A color version of this figure is available in the online journal.)

to be identical to one another and their apparent differences are attributed to the projection effect. The interpretation of the central feature, on the other hand, is much less straight forward. While there exist ostensible variations in the surface brightness, it is difficult to assert with any degree of certainty that it is shell-like. After experimenting with a couple of possible morphologies, including ones in which the central feature is shell-like and more or less perpendicular to the plane of the sky, we found that the model in which the central element has a bipolar structure with an uniform density distribution produces renderings that most closely resembles the *HST* observations. The 3D mesh and the *Shape* rendered image of the model is displayed in the center and right panel of Figure 7 respectively.

M 1-30. M 1-30 consists of two pairs of bipolar lobes. The observed complex *S*-shaped feature is emulated by the intersecting region of two bipolar elements. The bipolar components are constructed following the measured dimensions and P.A. listed in Table 2 and are assumed to lie on the plane of the sky. The waist of each bipolar cavity is then tightened according to the parameters provided in Table 3. Rendered from the 3D mesh shown in the center panel of Figure 8, the image displayed in the right panel successfully captures the characteristic *S*-shaped feature in the *HST* image.

M 1-59. M 1-59 consists of five bipolar elements that appear to exhibit shell-like features (left panel of Figure 9). We assume that the bipolar components are of equal lengths but with different widths. Differences in the apparent lengths seen in the observed images arise solely from the projection effect. Inclination of each element is derived from the measurements listed in Table 2. Specific parameters used in the model are given in Table 3. Using the 3D mesh in the center panel of Figure 9, we are able to simulate the observed structure of this nebula (right panel of Figure 9).

M 1-61. Four pairs of bipolar lobes can be identified from the *HST* image of M 1-61. Similar to M 1-59, the these bipolar components are assumed to be of identical absolute length but different widths. Their projected lengths, provided in Table 2, are used to derive the inclination of each element. The bipolar lobes in this PN are once again likely to be cavities; hence, they are modeled using a shell structure. The central feature, not shown in the 3D mesh in the center panel of Figure 10 to improve visibility, is emulated by carving out another pair of bipolar lobes from the halo component. Shown in the right panel of Figure 10, the *Shape* rendered image of M 1-61 display strong resemblance to the *HST* image. Features arising from the intersecting regions of the different components are also clearly visible in the rendering.

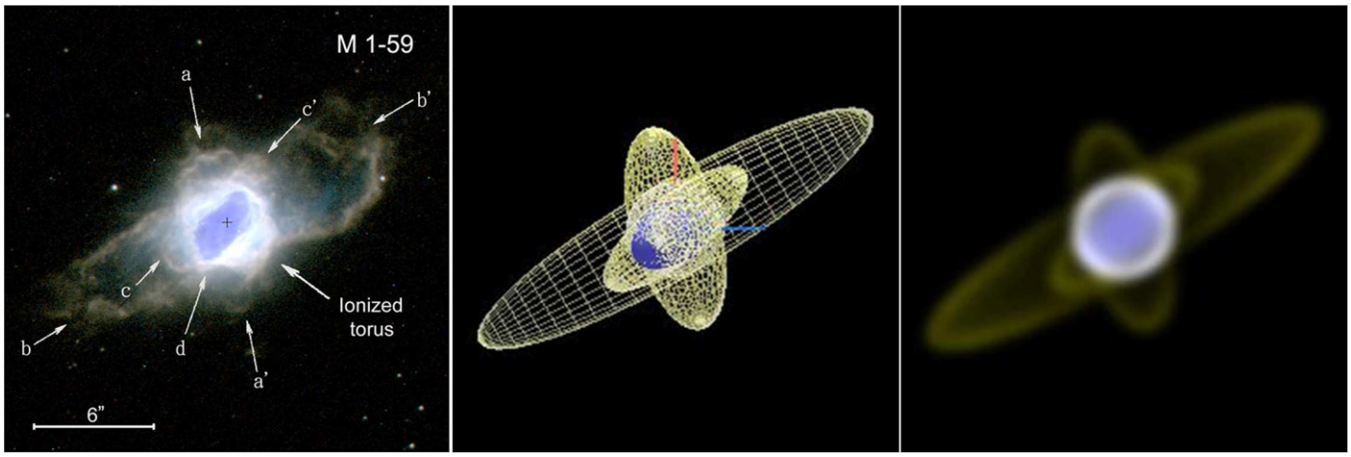

Figure 9. *HST* image (left), three-dimensional mesh (center), and rendered image (right) of M 1-59. A Gaussian blur has been applied to the rendering.
(A color version of this figure is available in the online journal.)

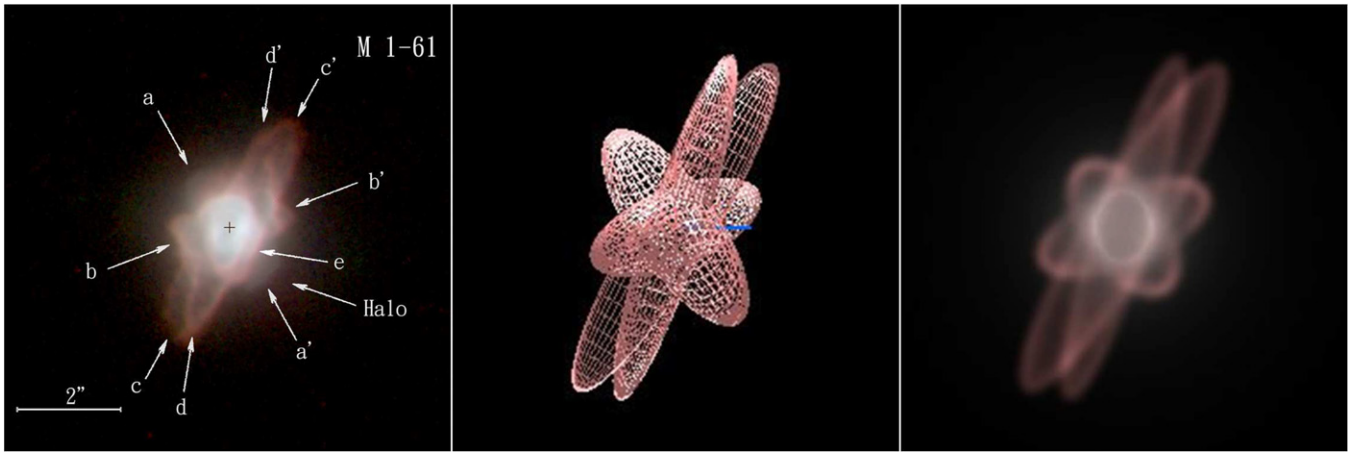

Figure 10. *HST* image (left), three-dimensional mesh (center), and rendered image (right) of M 1-61. The scattering halo is not shown in the mesh. A Gaussian blur has been applied to the rendering.
(A color version of this figure is available in the online journal.)

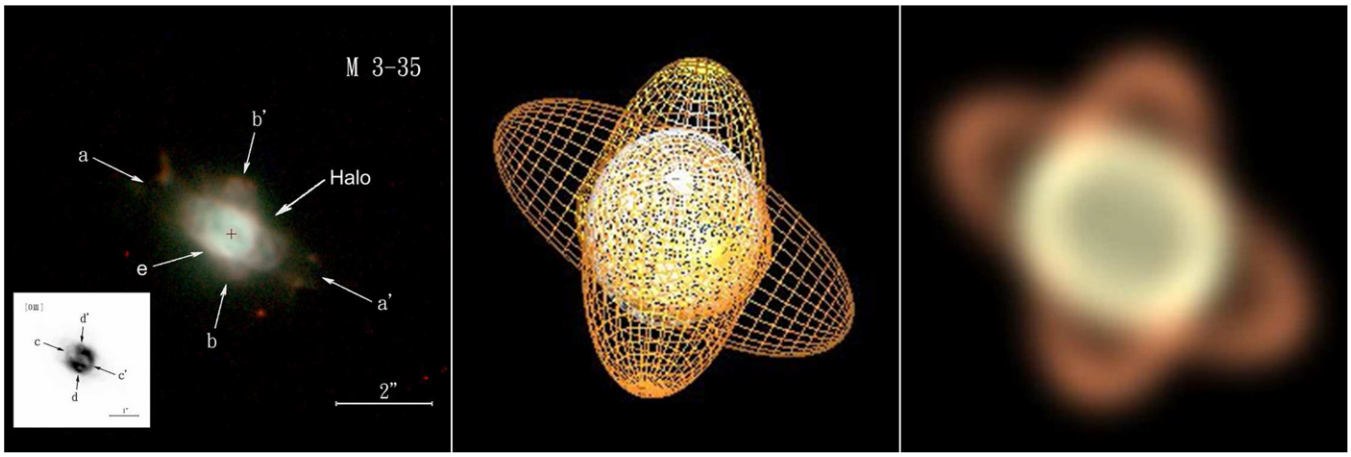

Figure 11. *HST* image (left), three-dimensional mesh (center), and rendered image (right) of M 3-35. A Gaussian blur has been applied to the rendering. The gray-scale insert shows the central cavity.
(A color version of this figure is available in the online journal.)

M 3-35. Two bipolar cavities are identified in the *HST* image of M 3-35. They are replicated in the *Shape* model using identical bipolar shell at the orientations listed in Table 3. Although the narrow band [O III] image seems to suggest another two pairs of bipolar lobes, the addition of such structure introduces inconsistencies in the rendering. To replicate the central feature, however, another bipolar component, identical to the other two, is introduced and is assumed to align on the line of sight. The resulting rendering, displayed in right panel of Figure 11 is in good agreement with the observation. Since a shell structure is not particularly obvious in the central feature, a model in which a uniform density distribution is assigned to the

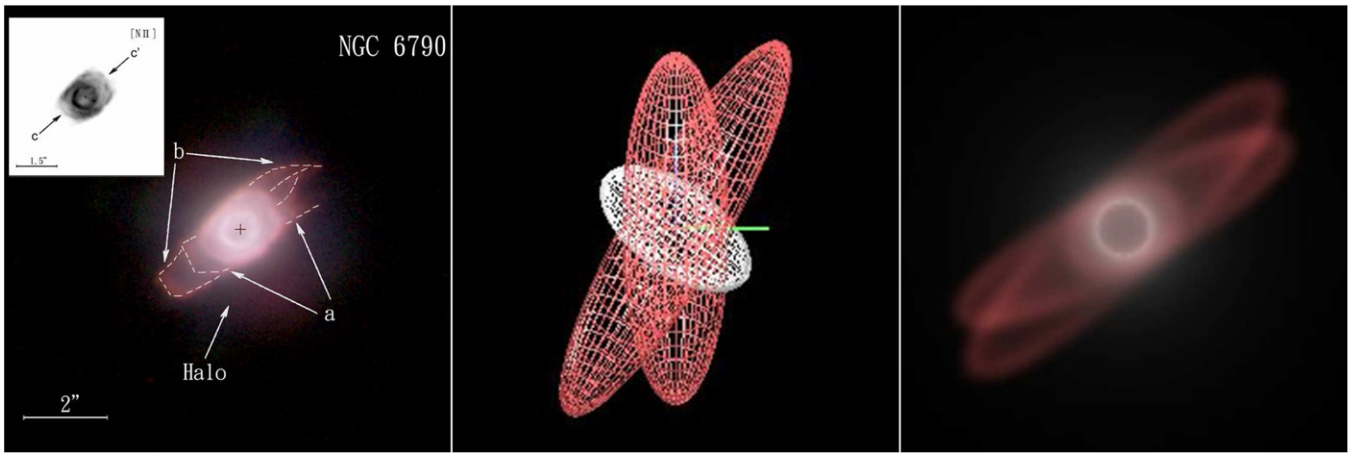

Figure 12. *HST* image (left), three-dimensional mesh (center) and rendered image (right) of NGC 6790. The scattering halo is not shown in the mesh. The mesh of the model is oriented to best display the three-dimensional morphology and is not related to the actual orientation of the PN with respect to the plane of the sky. A Gaussian blur has been applied to the rendering. The gray-scale insert shows the central cavity.

(A color version of this figure is available in the online journal.)

third bipolar component has also been created. The rendered image such a model, nonetheless, does not offer significant improvement as some surface brightness variation is visible in the central region of the *HST* image.

NGC 6790. As can be seen in the left panel of Figure 12, the outer region of the PN composes of two bipolar components. They are modeled using identical bipolar shells whose orientations are derived from measurements provided in Table 2. Elongation of the central feature rules out the possibility that it is formed by a single bipolar element that is oriented slightly off the line of sight. The central features must, therefore, be modeled using multiple elements. While the outer central feature is replicated using a third, smaller bipolar component, the innermost central feature is emulated by carving out a spherical cavity from the halo component. The rendered image in the right panel of Figure 12 not only shows strong resemblance with the *HST* image, features that arise from the intersection of the outer bipolar elements are also successfully replicated.

In our models, the lobes of each PN have approximately equal width-to-length ratios. If we assume that the width-to-length values are uniquely determined by the velocity of the outflow respect to the local sound speed, we can conclude that the outflows at different directions have nearly equal velocities.

5. DISCUSSIONS

Although at first glance many of the objects in our sample of compact PNs have simple elliptical or bipolar structures, careful examinations of the *HST* images have revealed new internal structures. Based on these observations, we would classify H 1-54, Hen 2-447, IC 5117, M 1-30, M 1-59, M 1-61, and M 3-35 (hereafter Class I) as multipolar nebulae with multiple pairs of bipolar lobes oriented at different directions. The other three objects: Hen 2-86, Hen 2-320, and NGC 6790 (hereafter Class II) all have multiple lobes aligned along almost the same direction. All objects possess point symmetry—meaning that all the multiple lobes have a common point of origin. The morphology of the Class I objects gives the impression that the lobes are the result of a precessing phenomena, and the Class II objects may be the result of consecutive ejections collimated by a similar mechanism.

All the Class I multipolar PNs exhibit a central cavity, which is even more pronounced than the lobes for some PNs (e.g., M 1-30). Central cavity of this type has not been seen in proto-PNs (see, e.g., Sahai et al. 2007) and the existence of these cavities may be the result of stellar evolution. After the stellar wind ceases, the increasing thermal pressure of the photoionized region becomes dominant. The expansion of the photoionized gas leads to the destruction of the multipolar lobes and other small-scale structures (García-Segura et al. 2006).

A slightly different scenario has been presented by Huarte-Espinosa et al. (2012), who successfully modeled the morphological transition from bipolar to elliptical by assuming that the systems begin with a jet flow (during the proto-PN phase) but are followed by a spherical fast wind (during the PN phase). Therefore, our observations may represent an evolution during the young PN age—the transition from a lobe-dominant to a cavity-dominant phase. Figure 13 shows a schematic diagram of the morphology transition. This is consistent with the observations that many young PNs show bipolar or multipolar structures while evolved PNs are mostly round or elliptical.

The observed lobes show sharp boundaries at their tips (e.g., H 1-54 and M 1-61) or/and along the lateral edges (e.g., Hen 1-320 and NGC 6790), suggesting that the lobes are confined by an external medium. The observed morphology of the lobes suggested that they represent low-density cavities carved out by colliminated fast winds.

Recent hydrodynamic simulations have shown that multipolar structures and secondary lobes can be naturally produced through the interaction between a fast wind and a highly inhomogeneous and filamentary shell (Steffen et al. 2013), and as a consequence, there is no need for a collimation mechanism of the outflow. We find that some of the PNs closely resemble the modeled results. For example, M1-59 and M1-61 display a pair of main lobes with less well-defined boundaries and a few secondary lobes and filamentary structures in the central regions. These morphological structures are similar to the modeled images of Steffen et al. (2013, Figures 6–11). The filamentary shell may be formed from instabilities of the photodissociation-shock front in the pre-PN stage, as suggested by García-Segura (2010). If this is case, the directions of the secondary lobes should be nearly random. The models are apparently not able to interpret the coaxial lobes of the Class II objects.

From the spectral energy distributions (SEDs) of these nebulae (Appendix), we do not find obvious difference between the SEDs of Class I and Class II objects. However, the SEDs of

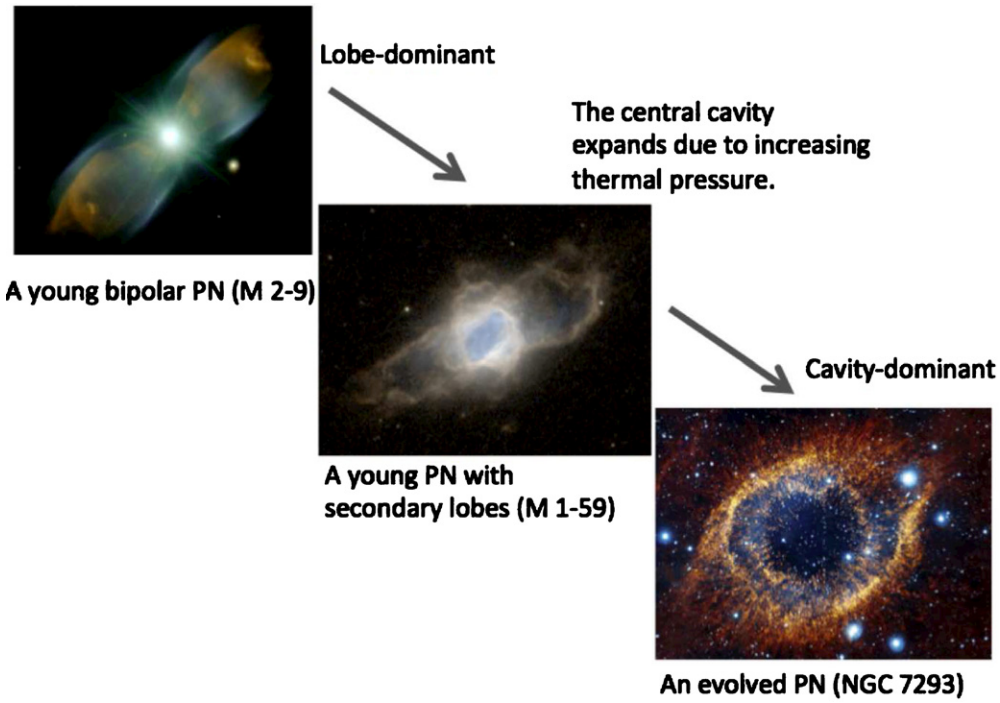

Figure 13. Schematic diagram of the morphology transition from lobe-dominant to cavity-dominant. The evolved PN NGC 7293 apparently exhibits vestiges of previous outflows.

(A color version of this figure is available in the online journal.)

Hen 2-86 and Hen 2-320 exhibit a steeper rise in the wavelength range from 5 to 30 μm than those of Class I PNs (Figure 13). This is conceivable in that differing from optical emission, the IR emission of the two PNs dominantly originates from a nearly edge-on torus, which is very optically thick so that the inner warm regions are largely obscured. The central torus could play an important role in collimating the outflows in Hen 2-86 and Hen 2-320. It has been suggested that many PNs with mixed dust chemistry exhibit point-symmetric structures (Stanghellini et al. 2012). This proposed correlation needs to be explored further by infrared spectroscopic observations.

6. CONCLUSIONS

Although a number of PNs with multipolar morphology have been reported recently (Manchado et al. 2011; Sahai et al. 2011), the results of this paper suggest that multipolar nebulae are much more common than previously thought. In the past, many multipolar PNs have been misclassified as "bipolar" or/and "elliptical." Examples of such misclassification include NGC 2440, NGC 6072 (Corradi & Schwarz 1995) and NGC 6644 (Stanghellini et al. 1993), but these objects are actually multipolar (López et al. 1998; Kwok et al. 2010; Hsia et al. 2010). It is possible the present sample of multipolar nebulae only represent the tip of the iceberg, as other bipolar/elliptical PNs may also be multipolar when deeper imaging reveals fainter structures.

Our sample of PNs are generally considered as young objects. It would be interesting to explore whether the multinebular properties are related to age. If the multinebular property is more common in young PNs, it could be the result of either the multipolar lobes are washed out/smoothed over by later dynamical processes, or the decreased surface brightness of the lobes in evolved PNs make them more difficult to detect.

From 3D simulations, we are able to reproduce the observed structures with a set of multiple bipolar lobes. One issue of creating 3D models from 2D images is its inherent degeneracy. As a result of the projection effect, different 3D structures can lead to the same apparent image. A way to break this degeneracy is to make use of position–velocity diagrams from imaging-spectroscopic observations. Unfortunately, there exist no kinematic data for most objects in this study. Even for the PNs with spatially resolved spectra available, the resolution is so poor that they can all be reproduced using uniform spheres with a Hubble flow. In spite of the possible non-uniqueness of these models, they do illustrate that the observed nebular structures of these objects need to be explained by multiple sets of geometric/kinematic components. These components are probably the result of interactions between multiple phases of mass loss, separated by time and/or a change in ejection directions. We hope that these observations will motivate further theoretical work on the dynamics of PNs.

We thank Nico Koning for helpful discussions on the SHAPE modeling. Some of the data presented in this paper were obtained from the Multimission Archive at the Space Telescope Science Institute (MAST). STScI is operated by the Association of Universities for Research in Astronomy, Inc., under NASA contract NAS5-26555. Support for MAST for non-*HST* data is provided by the NASA Office of Space Science via grant NAG5-7584 and by other grants and contracts. This work was partially supported by the Research Grants Council of the Hong Kong Special Administrative Region, China (project no. HKU 7031/10P.).

APPENDIX

SPECTRAL ENERGY DISTRIBUTION

One of the characteristics of young PNs is strong infrared excess. Since the dust component of PNs expands and cools as PN ages, the degree of infrared excess is largest in PNs

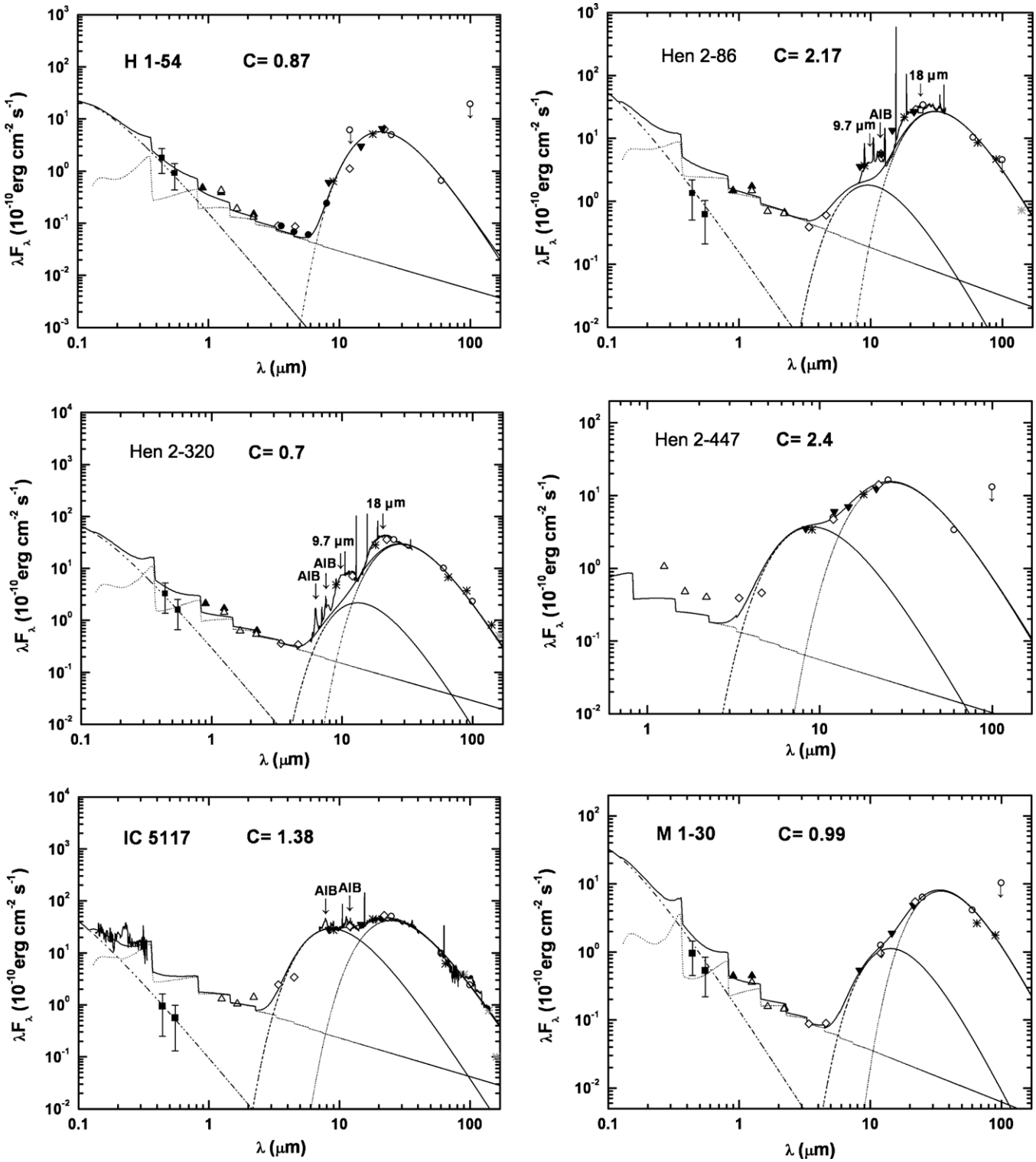

Figure 14. SEDs of 10 multipolar PNs in the *HST* sample. The filled squares are *B* and *V* photometry of the central stars. The filled and open triangles, filled circles, open diamonds, inverse filled triangles, open squares, open circles, and asterisks are from the DENIS, 2MASS, GLIMPSE, *WISE*, *MSX*, MIPSGAL, *IRAS*, and *AKARI* survey, respectively. The light asterisks represent the uncertain *AKARI* detections. Note that some fluxes measured from *IRAS* 12 and 100 μm are upper limits. When available, the *ISO* and *Spitzer* IRS spectra are also plotted. Some of the spectral features are marked. The three BB-like curves (from left to right) represent the central star, and the two dust components. The dotted lines are model curves for the nebular continuum emission. The total flux from all components are plotted as solid lines.

in their early stages of stellar evolution. Analysis of the SED of young PNs suggests that a significant fraction of their total energy output is in the infrared (Zhang & Kwok 1991). We have therefore constructed the SEDs of our sample objects using archival data and the results are shown in Figure 14. In the UV, we have taken data from the *International Ultraviolet Explorer* (*IUE*) low dispersion spectrograph. The *IUE* spectra of two objects (IC 5117 and NGC 6790) are extracted from the *IUE* Data Analysis Center (IUEDAC). In the infrared, the *Spitzer* Infrared Spectrograph (IRS) measurements and *Infrared*

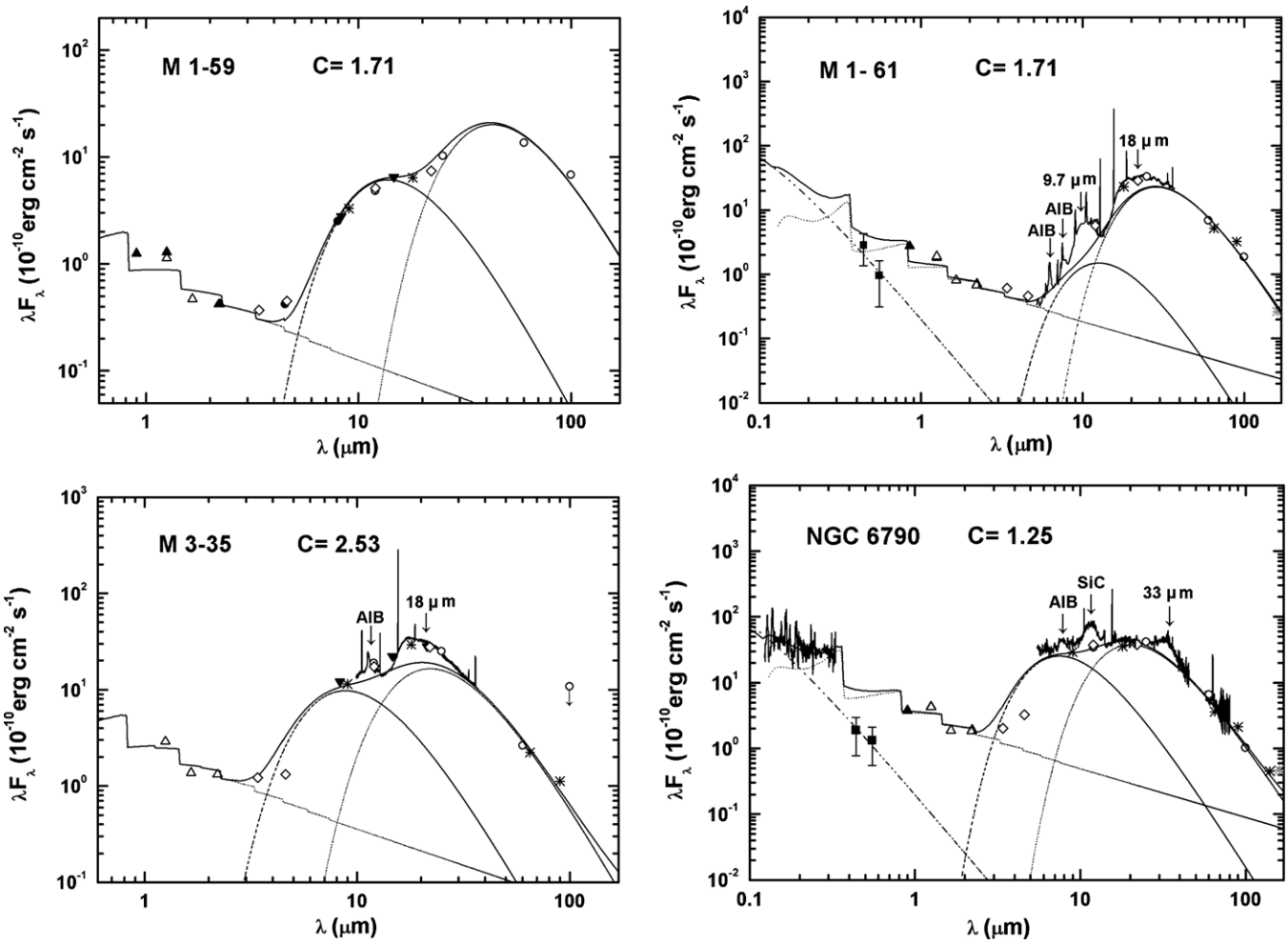

Figure 14. (Continued)

Space Observatory (*ISO*) observations are used. A journal of the *IUE*, *Spitzer* IRS, and *ISO* observations of these nebulae are given in Table 4. For photometric measurements, the optical *B* and *V* magnitudes of central stars of the nebulae are obtained from Shaw & Kaler (1985) and Tylenda et al. (1989, 1991), respectively. In the infrared, data are taken from the Deep Near-Infrared Southern Sky Survey (DENIS), Two Micron All Sky Survey (2MASS), *Midcourse Space Experiment* (*MSX*), *AKARI* (Tajitsu & Tamura 1998) and *Infrared Astronomical Satellite* (*IRAS*) catalogs. We have also made used of the a mid-infrared data from the *Spitzer* and *Wide-field Infrared Survey Explorer* (*WISE*; Wright et al. 2010) surveys to measure the integrated fluxes of the sample PNs using method described in Zhang & Kwok (2009) and Hsia & Zhang (2014). A summary of archival data used is given in Table 5. We note that some of the filters are broad, therefore color corrections and source aperture calibrations may be needed. The values for the color corrections and aperture calibration factors used in Figure 14 and Table 5 can be found in Wright et al. (2010) and Reach et al. (2005).

The nebular physical parameters of these objects are taken from the literature. The interstellar extinction coefficients are taken from Tylenda et al. (1989, 1991, 1992), Cahn et al. (1992), Shaw & Kaler (1985), and Girard et al. (2007). The Hβ fluxes are from Acker et al. (1992). The nebular electron densities (n_e) and electron temperatures (T_e) are taken from Tylenda et al. (1991), Cahn et al. (1992), Shaw & Kaler (1985), Stanghellini & Kaler (1989), and Zhang & Kwok (1991).

Table 4
IUE, IRS and *ISO* Observations

PN	Name	Instrument	Exposures (s)
		IUE spectra	
G 037.8-06.3	NGC 6790	SWP 15446	2100
		SWP 31831	3600
		SWP 15411	5400
		LWR 08709	1200
		LWR 11935	1500
		LWR 11922	3600
G 089.8-05.1	IC 5117	SWP 25835	1800
		SWP 31825	9000
		LWR 05883	1800
		LWR 05884	17700
		IRS observation	
G 019.4-05.3	M 1-61	AORkey 25837824	12.58
G 071.6-02.3	M 3-35	AORkey 18183424	14.68
G 300.7-02.0	Hen 2-86	AORkey 25853440	12.58
G 352.9-07.5	Hen 2-320	AORkey 11326464	12.58
		ISO spectra	
G 037.8-06.3	NGC 6790	TDTkey 53400762	766
		TDTkey 13401107	1062
		TDTkey 13401608	1330
G 089.8-05.1	IC 5117	TDTkey 36701824	1140
		TDTkey 36701822	1858

Table 5
Photometric Measurements

Filters	Objects									
	H 1-54	Hen 2-86	Hen 2-320	Hen 2-447	IC 5117	M 1-30	M 1-59	M 1-61	M 3-35	NGC 6790
					Central star					
B (mag)	15.7(1)	19.2(2)	14.4(1)	...	17.5(3)	16.6(1)	...	17.1(2)	...	16.3(2)
V (mag)	15.4(1)	18.4(2)	14.3(1)	...	16.7(3)	16.4(1)	...	16.8(2)	...	15.5(2)
					Nebula[a]					
DENIS I[b] (mag)	13.614	13.912	12.103	...	...	14.042	13.700	11.602	...	11.963
DENIS J[b] (mag)	12.668	11.942	11.330	...	...	12.921	12.250	11.529	...	10.598
DENIS K[b] (mag)	11.886	10.746	10.526	...	...	12.133	11.258	10.649	...	9.449
2MASS J[c] (mag)	12.703	12.155	11.516	12.803	11.297	13.163	12.328	12.785	11.844	10.610
2MASS H[c] (mag)	12.571	11.853	11.476	12.282	10.716	13.058	12.205	11.544	11.277	10.452
2MASS Ks[c] (mag)	11.851	10.789	10.720	11.211	9.488	12.184	11.225	10.594	10.105	9.469
SPITZER F 3.6 μm (mJy)	11.18	...	...	...	...	...	...	...	...	...
SPITZER F 4.5 μm (mJy)	12.33	...	...	...	...	...	62.26	...	...	...
SPITZER F 5.8 μm (mJy)	11.59	...	...	...	...	...	...	...	...	...
SPITZER F 8.0 μm (mJy)	63.54	...	...	...	...	...	610.73	...	...	...
SPITZER F 24 μm (mJy)	...	22.17	...	...	...	...	...	...	...	...
WISE F 3.4 μm (mJy)	10.12	43.84	40.25	37.46	278.43	9.97	42.91	92.34	138.26	229.31
WISE F 4.6 μm (mJy)	13.42	83.96	52.51	65.56	522.21	13.74	70.71	86.14	202.32	497.63
WISE F 12 μm (mJy)	446.53	2275.12	2859.34	1892.31	13056.11	385.33	2042.26	2311.37	6959.20	14935.59
WISE F 22 μm (mJy)	4680.31	21158.78	26295.30	10468.79	38714.54	3998.31	5294.27	21080.05	20374.48	27866.67
MSX F 8.28 μm[d] (Jy)	0.168	0.990	...	0.858	6.137	0.148	0.909	...	3.361	...
MSX F 12.13 μm[d] (Jy)	...	2.298	...	2.728	12.86:	...	...	...	6.855	...
MSX F 14.65 μm[d] (Jy)	1.216	6.542	...	3.453	17.26:	0.923	4.399	...	10.86	...
MSX F 21.3 μm[d] (Jy)	4.628	18.79	...	8.853	33.14	3.428	3.77	...	20.08	...
AKARI F 9 μm[e] (Jy)	0.192	1.102	1.441	0.951	6.447	...	0.899	...	3.437	6.636
AKARI F 18 μm[e] (Jy)	3.092	12.943	16.842	6.286	26.937	...	3.844	13.886	16.454	21.477
AKARI F 65 μm[e] (Jy)	...	18.480	14.692	...	13.535	5.714	...	11.311	4.837	7.792
AKARI F 90 μm[e] (Jy)	...	14.073	11.152	...	11.489:	5.292	...	9.759	3.650	6.359
AKARI F 140 μm[e] (Jy)	...	3.369:	4.286	...	3.659:	...	...	...	...	2.105
AKARI F 160 μm[e] (Jy)	...	...	3.226:	...	0.543:	...	...	1.401:	...	2.493:
IRAS F 12 μm[f] (Jy)	<2.43	2.23	3.54	2.37	13.58	<0.50	1.61	2.46	7.60	13.81[g]
IRAS F 25 μm[f] (Jy)	4.16	29.82	31.21	13.71	46.15	6.05	7.79	27.73	20.96	34.90[g]
IRAS F 60 μm[f] (Jy)	1.31	20.74	16.82	6.82	19.69	7.81	24.26	13.84	5.23	13.10[g]
IRAS F 100 μm[f] (Jy)	<64.19	<15.21	7.17	<43.52	8.04	<34.55	26.69	5.29	<36.02	3.40[g]

Notes.
[a] The colon represents uncertain detection. For some *IRAS* measurements, the fluxes measured from 12 μm and 100 μm are upper limits.
[b] From DENIS database.
[c] From 2MASS point source catalog.
[d] From *MSX* infrared point source catalog.
[e] From *AKARI* all sky survey point source catalog.
[f] From Tajitsu & Tamura (1998), the color- and diameter-corrected *IRAS* fluxes were given.
[g] From *IRAS* point source catalog.
References. (1) Tylenda et al. 1991; (2) Tylenda et al. 1989; (3) Shaw & Kaler 1985.

The abundances of He^{2+}/H^+ and He/H of these PNs are taken from Preite-Martinez et al. (1989), Cahn et al. (1992), Shaw & Kaler (1985), and Zhang & Kwok (1991). After correcting their UV spectrum and corresponding optical measurements by the extinction values (which accounts for both circumstellar and interstellar extinction), the emergent fluxes of these objects can be then fitted by using the same expressions as Hsia et al. (2010). The SEDs of these PNs corrected for extinction are shown in Figure 14.

We can see that these SEDs clearly separate the contributions from different components including photospheric continuum of the central star (except Hen 2-447, M 1-59, and M 3-35), the nebular continuum from ionized gas, and the dust thermal emission. The observed dust emission is too broad to fitted by a single blackbody and the observed spectrum is therefore fitted by two modified blackbodies of different temperatures, corresponding to a warm (T_{wd}) and a cold (T_{cd}) dust components. Using the assumed distances (D) listed in Column 13 of Table 6, we can derive a number of physical parameters such as minimum luminosity of the central star (L_*), the total mass of dust components (M_d), and the mass of ionized gas (M_i). The dust mass is derived from the infrared flux emitted by the dust component, and the ionized mass is derived based on a fitting of the bound–free and free–free continuum. The dust particles are assumed to have an emissivity of $Q_\lambda = Q_0(\lambda/\lambda_0)^{-\alpha}$, where $\lambda_0 = 1\,\mu$m, $Q_0 = 0.1$, and α has values between 1 and 1.3. The kinematic ages of these PNs can also be estimated by their apparent sizes of the longest lobes (assuming the lobes lie close to the plane of the sky), distances, and expansion velocities (V_{exp}). A summary of the derived properties of these objects is given in Table 6. The names of these PNs are listed in Column 1. The derived effective temperatures of central

Table 6
Physical Properties of the Sample Nebulae

Object	T_*[a] (10^3 K)	$T_{*,\rm ref}$ (10^3 K)	$T_{\rm wd}$[a] (K)	$T_{\rm cd}$[a] (K)	log L_*[a] ($L_\odot$)	M_d[a] ($M_\odot$)	M_i[a] ($M_\odot$)	M_d/M_i	Class[b]	θ[c] ($''$)	$V_{\rm exp}$[d] (km s^{-1})	D (kpc)	Age[e] (yr)
H 1-54	43 ± 5	41.3[(1)], 39[(2)]	...	136	3.77	9.90×10^{-5}	0.04	2.48×10^{-3}	O[(5)]	1.58	22	8.01[(10)]	2730
Hen 2-86	72.5 ± 8.7	67[(2)], 88[(2)]	312	96	3.74	7.14×10^{-4}	0.15	4.76×10^{-3}	M[(6)]	5.23	22	3.58[(10)]	4040
Hen 2-320	53 ± 7	49[(2)]	208	97	3.76	8.51×10^{-4}	0.09	9.46×10^{-3}	M[(7)]	4.95	22	4.44[(10)]	4750
Hen 2-447	...	...	298	103	...	6.04×10^{-4}	0.10	6.04×10^{-3}	M[(8)]	2.40	22	6.30[(10)]	3260
IC 5117	88.5 ± 7.5	76[(3)], 90[(3)]	335	117	3.84	4.43×10^{-4}	0.16	2.77×10^{-3}	C[(9)]	1.78	21.5	3.83[(10)]	1510
M 1-30	56 ± 7.3	48[(2)], 61[(2)]	203	84	3.75	9.18×10^{-4}	0.09	1.02×10^{-2}	...	2.29	22	5.58[(11)]	2760
M 1-59	...	...	211	68	...	3.29×10^{-4}	0.02	1.65×10^{-2}	...	9.02	13[f]	1.23[(12)]	4050
M 1-61	69 ± 6.2	67[(2)], 72.5[(1)]	217	96	3.87	7.98×10^{-4}	0.58	1.38×10^{-3}	M[(6)]	2.52	22	4.73[(10)]	2570
M 3-35	...	...	323	129	...	1.30×10^{-4}	0.33	3.93×10^{-4}	M[(9)]	1.43	30	4.44[(10)]	1370
NGC 6790	80.5 ± 7.6	76[(3)], 85[(4)]	381	154	3.88	9.74×10^{-5}	0.14	6.96×10^{-4}	M[(8)]	2.34	22	3.18[(10)]	1610

Notes.
[a] Derived from SED fitting.
[b] O: oxygen-rich dust, M: mixed-chemistry dust, C: carbon-rich dust.
[c] The angular radius of the longest lobe of this object assuming all lobes have similar projected sizes on the sky.
[d] Expansion velocity measured from [N II] λ6584 (Acker et al. 1992).
[e] Due to the inclination effect in a 2D projection model and global geometry of the expanding structures, the derived kinematic ages here are the upper limits.
[f] Expansion velocity measured from [O III] λ5007 (Acker et al. 1992).
References. (1) Zhang & Kwok 1991; (2) Gleizes et al. 1989; (3) Kaler & Jacoby 1991; (4) Aller et al. 1996; (5) Casassus et al. 2001a; (6) Stanghellini et al. 2012; (7) This study; (8) Casassus et al. 2001b; (9) Rinehart et al. 2002; (10) Zhang 1995; (11) Phillips 2005; (12) Acker et al. 1992.

stars (T_*) from SED fittings and those obtained from the references for comparison ($T_{*,\rm ref}$) are given in Columns 2 and 3. Columns 4–6 give the temperatures of warm and cool dust components, and the derived luminosities of the central stars of these PNs, respectively. The total mass of the warm and cold dust components, the derived ionized mass, and the dust-to-ionized gas mass ratios (M_d/M_i) are given in Columns 7–9. Column 10 gives their dust grain classes based on spectral information. The angular radii of the longest lobes (θ) of these objects measured from Hα images are listed in Column 11. Columns 12–14 give their expansion velocities, distances, and the derived kinematic ages. Because of the uncertain extinction correction of each object for the visible photometry of the central star, and the fact that these photometric data lie in the Rayleigh–Jeans side of the blackbody curve, the temperature of central star can not be determined precisely. Even so, our estimates of T_* are consistent with values previously reported in the literature (see Table 6).

The derived values of M_d/M_i for our sample objects are generally within the range of dust-to-gas mass ratios (10^{-2}–10^{-3}) typically found in PNs (Stasińska & Szczerba 1999). We note that these values should be considered as the maximum for the actual dust-to-gas ratios since part of the gas in the nebulae is likely to be in molecular (non-ionic) form. Considering the uncertain determinations of projected sizes and measured expansion velocities of the PNs caused by the inclination effect in a 2D projection model and global geometry of the expanding structures, our derived kinematic ages used here are just rough, order-of-magnitude estimates. We find that most of these PNs are quite young, with a median age of 2740 yr. The expansion velocities of multipolar PNs in the lobes are usually found to be larger than that in the central region, thus the derived kinematic ages here are likely to be the upper limits.

REFERENCES

Aaquist, O. B., & Kwok, S. 1990, A&AS, 84, 229
Aaquist, O. B., & Kwok, S. 1991, ApJ, 378, 599
Acker, A., Ochsenbein, F., Stenholm, B., et al. 1992, Strasbourg-ESO Catalog of Galactic Planetary Nebulae, Parts I and II (Garching: European Southern Observatory)
Aller, L. H., & Czyzak, S. J. 1983, ApJS, 51, 211
Aller, L. H., Hyung, S., & Feibelman, W. A. 1996, PASP, 108, 488
Balick, B., & Frank, A. 2002, ARA&A, 40, 439
Cahn, J. H., Kaler, J. B., & Stanghellini, L. 1992, A&AS, 94, 399
Casassus, S., Roche, P. F., Aitken, D. K., et al. 2001a, MNRAS, 327, 744
Casassus, S., Roche, P. F., Aitken, D. K., et al. 2001b, MNRAS, 320, 424
Clark, D. M., López, J. A., Steffen, W., et al. 2013, AJ, 145, 57
Corradi, R. L. M., Livio, M., Balick, B., et al. 2001, ApJ, 553, 211
Corradi, R. L. M., Sánchez-Blázquez, P., Mellema, G., et al. 2004, A&A, 417, 637
Corradi, R. L. M., & Schwarz, H. E. 1995, A&A, 293, 871
de Freitas Pacheco, J. A., Maciel, W. J., & Costa, R. D. D. 1992, A&A, 261, 579
García-Segura, G. 1997, ApJL, 489, L189
García-Segura, G. 2010, A&A, 520, L5
García-Segura, G., López, J. A., Steffen, W., Meaburn, J., & Manchado, A. 2006, ApJL, 646, L61
Girard, P., Köppen, J., & Acker, A. 2007, A&A, 463, 265
Gleizes, F., Acker, A., & Stenholm, B. 1989, A&A, 222, 237
Górny, S. K., Schwarz, H. E., Corradi, R. L. M., et al. 1999, A&AS, 136, 145
Guerrero, M. A., & Manchado, A. 1998, ApJ, 508, 262
Guerrero, M. A., Villaver, E., Manchado, A., et al. 2000, ApJS, 127, 125
Guillén, P. F., Vázquez, R., Miranda, L. F., et al. 2013, MNRAS, 432, 2676
Hsia, C.-H., Kwok, S., Zhang, Y., et al. 2010, ApJ, 725, 173
Hsia, C.-H., & Zhang, Y. 2014, A&A, 563, A63
Hua, C. T., Grundseth, B., & Maucherat, A. J. 1993, A&AS, 101, 541
Huarte-Espinosa, M., Frank, A., Balick, B., et al. 2012, MNRAS, 424, 2055
Kaler, J. B. 1986, ApJ, 308, 322
Kaler, J. B., & Jacoby, G. H. 1991, ApJ, 372, 215
Kwok, S. 1990, MNRAS, 244, 179
Kwok, S., & Aaquist, O. B. 1993, PASP, 105, 1456
Kwok, S., Chong, S.-N., Hsia, C.-H., et al. 2010, ApJ, 708, 93
Kwok, S., & Hsia, C.-H. 2007, ApJ, 660, 341
Kwok, S., & Su, K. Y. L. 2005, ApJ, 635, 49
Lee, T.-H., & Kwok, S. 2005, ApJ, 632, 340
López, J. A., Meaburn, J., Bryce, M., et al. 1998, ApJ, 493, 803
López, J. A., Vázquez, R., & Rodríguez, L. F. 1995, ApJL, 455, L63
Manchado, A., García-Hernández, D. A., Villaver, E., & Guironnet de Massas, J. 2011, in ASP Conf. Ser. 445, Why Galaxies Care About AGB Stars II, ed. F. Kerschbaum, T. Lebzelter, & B. Wing (San Francisco, CA: ASP), 161
Manchado, A., Stanghellini, L., & Guerrero, M. A. 1996, ApJ, 466, 95
Mampaso, A., Corradi, R. L. M., Viironen, K., et al. 2006, A&A, 458, 203
Phillips, J. P. 2005, MNRAS, 362, 847
Preite-Martinez, A., Acker, A., Köppen, J., et al. 1989, A&AS, 81, 309
Reach, W. T., Megeath, S. T., Cohen, M., et al. 2005, PASP, 117, 978
Rinehart, S. A., Houck, J. R., Smith, J. D., et al. 2002, MNRAS, 336, 66
Roeser, S., Demleitner, M., & Schilbach, E. 2010, AJ, 139, 2440
Sahai, R. 2000, ApJL, 537, L43

Sahai, R., Morris, M., Sánchez Contreras, C., & Claussen, M. 2007, AJ, 134, 2200
Sahai, R., Morris, M. R., & Villar, G. G. 2011, AJ, 141, 134
Shaw, R. A., & Kaler, J. B. 1985, ApJ, 295, 537
Stanghellini, L., Corradi, R. L. M., & Schwarz, H. E. 1993, A&A, 279, 521
Stanghellini, L., García-Hernández, D. A., García-Lario, P., et al. 2012, ApJ, 753, 172
Stanghellini, L., & Kaler, J. B. 1989, ApJ, 343, 811
Stasińska, G., & Szczerba, R. 1999, A&A, 352, 297
Steffen, W., Koning, N., Esquivel, A., et al. 2013, MNRAS, 436, 470
Steffen, W., Koning, N., Wenger, S., Morisset, C., & Magnor, M. 2011, IEEE Trans. Vis. Comput. Graphics, 17, 454
Tajitsu, A., & Tamura, S. 1998, AJ, 115, 1989
Terzian, Y., & Hajian, A. R. 2000, in ASP Conf. Ser. 199, Asymmetrical Planetary Nebulae II: From Origins to Microstructures, ed. J. H. Kastner, N. Soker, & S. Rappaport (San Francisco, CA: ASP), 33
Tylenda, R., Acker, A., Gleizes, F., et al. 1989, A&AS, 77, 39
Tylenda, R., Acker, A., Raytchev, B., et al. 1991, A&AS, 89, 77
Tylenda, R., Acker, A., Stenholm, B., et al. 1992, A&AS, 95, 337
Wright, E. L., Eisenhardt, P. R. M., Mainzer, A. K., et al. 2010, AJ, 140, 1868
Zhang, C. Y. 1995, ApJS, 98, 659
Zhang, C. Y., & Kwok, S. 1991, A&A, 250, 179
Zhang, Y., & Kwok, S. 2009, ApJ, 706, 252